Nano Research

ISSN 1998-0124 CN 11-5974/O4
https://doi.org/10.26599/NR.2025.94907300

Research Article

High-temperature shock-induced transformation of bulk copper into single-atom catalyst

Renjie Fang[1,§], Ji Yang[1,§], Wei-Shen Song[1], Na Yang[2], Jie Ding[3], Jian-Feng Li[1](✉), Feng Ru Fan[1](✉)

[1] State Key Laboratory of Physical Chemistry of Solid Surfaces, College of Chemistry and Chemical Engineering, Innovation Laboratory for Sciences and Technologies of Energy Materials of Fujian Province (IKKEM), Xiamen University, Xiamen 361005, China

[2] School of Materials and Energy, University of Electronic Science and Technology of China, Chengdu 611731, China

[3] Faculty of Chemistry and Food Chemistry & Center for Advancing Electronics Dresden (CFAED), Dresden University of Technology, Dresden 01062, Germany

[§] Renjie Fang and Ji Yang contributed equally to this work.

Nano Res., **Just Accepted Manuscript** • https://doi.org/10.26599/NR.2025.94907300

https://www.sciopen.com/journal/1998-0124 on Feb. 12, 2025

Just Accepted

TABLE OF CONTENTS (TOC)

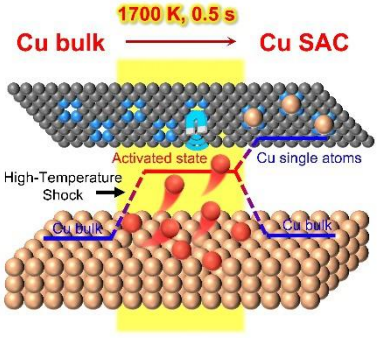

The high-temperature shock (HTS) strategy enables the direct transformation of bulk copper (Cu) foil into single atoms in just 0.5 seconds at 1700 K. The transient high temperature not only promotes the formation of thermodynamically favorable Cu-N bonds but also prevents excessive sintering and aggregation of metal atoms.

Nano Research

Open Access

Research Article

High-temperature shock-induced transformation of bulk copper into single-atom catalyst

Renjie Fang[1,§], Ji Yang[1,§], Wei-Shen Song[1], Na Yang[2], Jie Ding[3], Jian-Feng Li[1] ✉, and Feng Ru Fan[1] ✉

[1] *State Key Laboratory of Physical Chemistry of Solid Surfaces, College of Chemistry and Chemical Engineering, Innovation Laboratory for Sciences and Technologies of Energy Materials of Fujian Province (IKKEM), Xiamen University, Xiamen 361005, China*
[2] *School of Materials and Energy, University of Electronic Science and Technology of China, Chengdu 611731, China*
[3] *Faculty of Chemistry and Food Chemistry & Center for Advancing Electronics Dresden (CFAED), Dresden University of Technology, Dresden 01062, Germany*
[§] *Renjie Fang and Ji Yang contributed equally to this work.*

Received: 3 December 2024; **Revised:** 16 January 2025; **Accepted:** 12 February 2025

✉ Address correspondence to Jian-Feng Li, Li@xmu.edu.cn; Feng Ru Fan, frfan@xmu.edu.cn

Cite this article: *Nano Research*, 2025, 18, 94907300. https://doi.org/10.26599/NR.2025.94907300

ABSTRACT: Transforming nanoscale and bulk metals into single atoms is crucial for the scalable production of single-atom catalysts (SACs), especially during pyrolysis. However, conventional equilibrium heating approaches often require prolonged operation to decompose metal aggregates, leading to tedious and time-consuming procedures for synthesizing SACs. In this study, we introduce high-temperature shock (HTS) strategy to enhance metal atomization, achieving the direct transformation of bulk copper (Cu) foil into single atoms in just 0.5 seconds at 1700 K. The HTS-produced Cu catalyst demonstrates a high content of 0.54 wt%, comparable to those achieved by commonly reported top-down strategies, indicating that the HTS method provides a compelling alternative for synthesizing Cu SACs from bulk Cu precursors. Structural analysis confirmed the synthesis of a Cu-N-C SAC with a Cu-N_4 coordination environment. This Cu-N_4 structure shows excellent catalytic performance for nitrite reduction to ammonia, achieving over 90% Faradaic efficiency across the entire working potential range and an ammonia production rate of up to 11.12 mg cm^{-2} h^{-1} at -1.2 V vs. RHE, surpassing other reported Cu-based electrocatalysts. Furthermore, *ab initio* molecular dynamics (AIMD) simulations reveal that transient high temperatures not only promote the formation of thermodynamically favorable Cu-N bonds but also prevent excessive sintering and aggregation of metal atoms.

KEYWORDS: single-atom catalyst, bulk metal foil, high-temperature shock, rapid conversion, ammonia electrosynthesis

1. Instruction

In the past decade, single-atom catalysts (SACs) have attracted widespread attention and have emerged as one of the most active research frontiers in heterogeneous catalysisv [1-3]. Intensive efforts have been devoted to the development of high-performance SACs [4-5]. Among the established strategies, pyrolysis has been regarded as one of the most common ways to convert inactive precursors into highly active structure. For example, pyrolytic transformation of the mixture of metal-, carbon-, and nitrogen-precursors has shown great potential in preparing metal-nitrogen-carbon (M-N-C) SACs with high reactivity [6-7]. However, the aggregation of single atoms into clusters at elevated temperature, due to high surface free energy, remains a major challenge [8-11]. Such aggregates not only reduce the efficiency of metal atoms but also often leads to undesired side reactions. Therefore, the transformation of metal particles into single atoms is essential for synthesizing highly efficient SACs and remains a significant challenge.

Recent studies have shown that ultrafine metal particles (about 2 nm) produced by pyrolysis could be re-dispersed into single atoms (Fig. 1(a)). Wu et al. discovered that iron (Fe) and cobalt (Co) nitrate salts supported on N-C initially aggregate into corresponding oxides, with some clusters and a few single atoms at temperatures between 673 and 973 K. Beyond 973 K, disaggregation occurs, resulting in smaller clusters and single atoms [12-13]. This dynamic behavior of small particles transitioning to single atoms was interpreted as a thermal-induced dispersion mechanism. However, external heat input alone is insufficient to re-disperse larger metal precursors due to their high cohesive energy, and heating often leads to severe metal sintering. To overcome these limitations, chemical reaction-assisted pyrolysis has been employed to transform larger particles and bulk metal materials into mobile intermediates, which are then captured by the support with abundant anchoring sites (Fig. 1(b)) [14-16]. For instance, Qu and Yang et al. developed an atom-trapping method to directly transform commercial Cu_2O powder and bulk Cu foam into SACs [17-18]. This approach was enabled by ammonia-assisted thermolysis at high temperatures, which produced volatile $Cu(NH_3)_x$

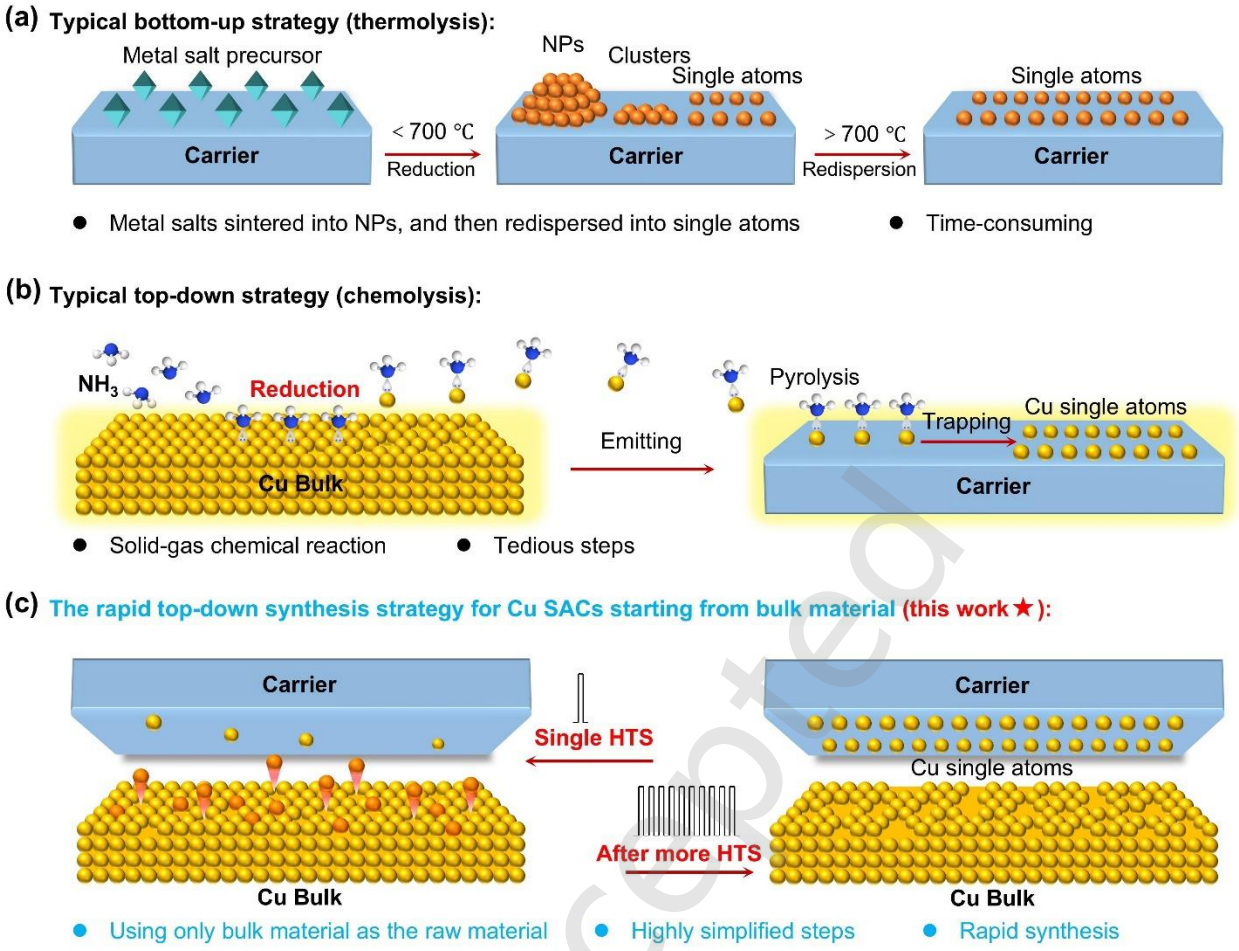

Figure 1. Comparison of different strategies for the synthesis of SACs. (a) Typical bottom-up strategies using wet chemical methods. (b) Typical thermochemical gas-assisted method for synthesizing Cu SAC. (c) Our proposed top-down strategy, where high-temperature shock (HTS) directly processes bulk copper to synthesize Cu SAC. (Blue, nitrogen atoms; white, hydrogen atoms; orange, iron atoms; yellow: copper atoms).

intermediates that were then trapped by a nitrogen-rich carbon substrate. Additionally, this chemical reaction-mediated re-dispersion process has also demonstrated that Cu nanoparticles can dynamically disaggregate into atomically dispersed Cu species at room temperature by reacting with hydroxyl species at room temperature [19-20].

However, these proposed dispersion strategies are kinetically sluggish, often requiring several hours or even days for larger particles and bulk metal materials. The high toxicity and strong corrosiveness of NH_3 also hinder the potential scale-up production of SACs. Therefore, developing a novel methodology for the rapid and scalable production of SACs from particle or bulk metal precursors would represent a significant advancement. As a newly developed synthetic technique, the high-temperature shock (HTS) heating method has been widely used to explore the controlled synthesis of thermodynamically metastable and high-performance solid catalyst materials, such as high-entropy alloys [21], clusters [22], and SACs [23-25]. This capability is attributed to its ultra-high heating and cooling rates, typically exceeding 1000 K/s, which facilitate the creation of kinetically-driven and thermodynamically non-equilibrium environments [26-27]. The high heating temperature and short duration in the HTS process have an intensive effect on achieving highly dispersed catalysts. The rapid heating rate activates precursors into an active state, while the short heating time prevents the aggregation of single atoms into particles [28]. Therefore, HTS is often observed in converting mononuclear metal precursors into single atoms. HTS has also gained attention for synthesizing various SACs, such as Pt, Ni, and Co, from their precursors [29-34]. However, the use of HTS to disaggregate metal particles or bulk precursors into SACs has been scarcely reported.

In this work, as depicted in Fig. 1(c), we report the first example of HTS transforming Cu foil into single atoms within 0.5 seconds at 1700 K. Inductively coupled plasma-optical emission spectrometer (ICP-OES) analysis determined a Cu content of up to 0.54 wt%, approaching the values recently reported for Cu SACs synthesized from bulk materials using top-down methods. The HTS-produced Cu single atoms, which coordinate with four nitrogen atoms, were characterized by aberration-corrected high-angle annular dark-field scanning transmission electron microscopy (HAADF-STEM) and X-ray absorption fine spectroscopy (XAFS). Catalytic evaluation for nitrite reduction to ammonia showed that the HTS-produced Cu single atoms exhibited a high Faradaic efficiency of over 90% across the working potential range, with an excellent production rate of 11.12 mg cm^{-2} h^{-1} at -1.2 V vs. RHE. Moreover, *ab initio* molecular dynamics (AIMD) simulations provided insights into the

formation process of single atoms, demonstrating that this transient process ensures atom activation, defect trapping, and prevents the sintering of single atoms. In addition, other types of metal including Fe, Co foil, and Cu foam have been used as precursors, demonstrating the generality of HTS for the synthesis of highly dispersed catalysts. This work not only presents a novel and rapid top-down strategy for synthesizing SACs, but also accelerates the practical deployment of converting bulk materials directly into SACs for large-scale production.

2 Results and discussion

2.1. High-Temperature Shock (HTS) Synthesis for Cu SAC

The corresponding synthetic process in the reaction chamber is depicted in Fig. 2(a), which schematically illustrates the synthesis of SACs, including the assembly of a sandwich structure of bulk metal loaded onto a defect-rich substrate, followed by periodic high-temperature shock treatment (Fig. S1). The latter step is a crucial part of the synthetic process. As illustrated in Fig. 2(b), an electrical input of 0.5 seconds raises the temperature to approximately 1750 K (Fig. S2), followed by rapid quenching during the off-state for a 5-second period. This setup allows for precise programming of heating temperature, pulse time, and repeated cycles [35-36]. The high temperature and short duration are key factors in the successful formation of a highly dispersed catalyst. As proposed in Fig. 2(c), the metal atoms evolve into an active state during HTS treatment and are subsequently trapped by nitrogen-defect ligands, generating thermally stable SACs. Additionally, the short heating time prevents the undesired agglomeration of the formed single atoms into metallic clusters, while also avoiding metal distortion due to melting during prolonged heating. After HTS synthesis, the spent bulk metal can be recycled as raw material for subsequent processes.

To demonstrate this approach, we chose a nitrogen-doped carbon substrate and Cu foil as model materials to prepare Cu single atoms (referred to as Cu-N-C-HTS). Details of the HTS experimental procedures are provided in the Methods section of the Supporting Information. The programmable nature of HTS allows for accurate tuning of synthetic parameters by adjusting the electric power input, such as the duration of a single heating pulse, temperature, and repeated cycles.37 The Cu loading results as a function of shocking time are displayed in Fig. 2(d) and Table S1. It can be seen that the Cu content initially increases and then decreases, reaching a peak value of 0.54 wt% at a 0.5-second pulse time. The observed decrease in Cu content at longer pulse times can be attributed to the melting of the Cu foil, as indicated in Fig. S3(a), due to the operating temperature exceeding the melting point of Cu (1358 K).

The Cu loading profile in Fig. S4 also exhibits a similar trend for the synthesis of Cu-N-C-HTS, showing a volcano-shaped distribution with respect to temperature. Specifically,

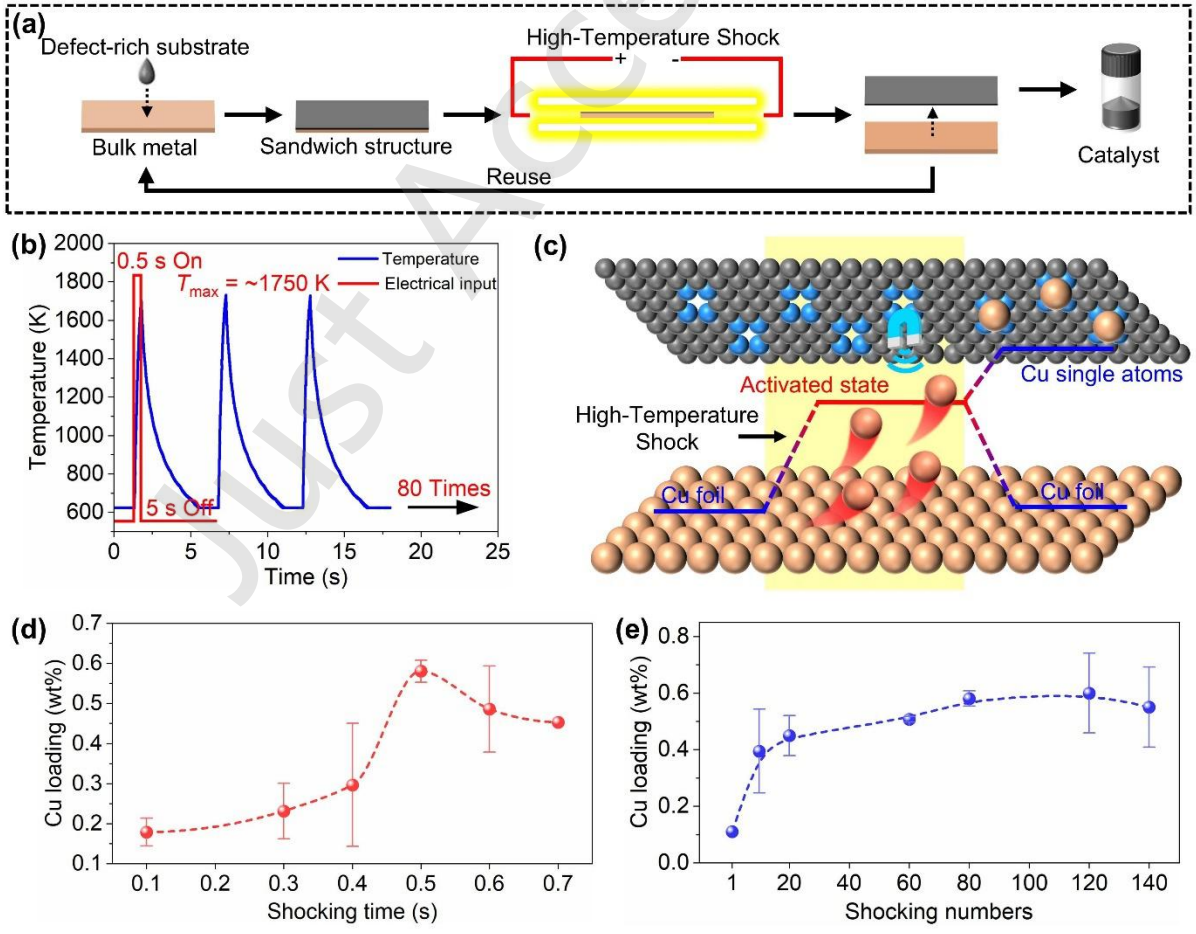

Figure 2. The synthetic illustration of SAC from bulk metal. (a) The HTS schematic of Cu-N-C-HTS SAC from bulk Cu foil (2 mm thick, 20 mm length and 5 mm width). (b) Temperature evolution during the HTS synthesis. (c) Proposed synthetic mechanism for the transformation of Cu foil to SAC. (d) Shocking time, and (e) shocking numbers-dependent Cu mass weight profiles.

when the temperature is between 1300 and 1500 K, the Cu content grows gradually. However, with an increase from 1500 to 1700 K, the Cu content is enhanced from 0.1 to 0.54 wt%, an almost fivefold increase. In contrast, further increasing the temperature to 1800 K led to a significant decrease in Cu loading, accompanied by severe deformation of the Cu foil (Fig. S3(b)). In addition to shocking time and pulse temperature, the number of shocking cycles was also precisely programmed for HTS synthesis. Fig. 2€ presents a profile of Cu loading as a function of the number of shocking cycles. Between 1 and 10 HTS cycles, Cu loading increases rapidly with the number of cycles, while after 10 HTS cycles, the rate of increase significantly slows down, and the Cu loading stabilizes after 80 HTS cycles. The corresponding spent metal foil after HTS is shown in Fig. S3(c). Raman spectroscopy of products from different HTS cycles demonstrates that as the number of HTS cycles increases, the number of N defects on the support decreases, leading to a gradual reduction in the rate of increase of Cu loading on Cu-N-C-HTS, which eventually stabilizes (Fig. S5) [38]. Notably, HAADF-STEM images of the product after 140 extreme HTS cycles demonstrated that copper species were uniformly dispersed as single atoms on the support surface without aggregation into clusters or particles (Fig. S6). Relevant loading data can be found in Table S1. In addition, the effect of the thickness of the deposited support on Cu loading was also investigated (Fig. S7). To the best of our knowledge, the obtained Cu loading of 0.54 wt% using HTS is comparable to values reported for top-down methods, such as the abrasion method (0.55 wt%) [39], atom trapping from Cu foam (0.54 wt%) [18], and Cu_2O powder (0.45 wt%) [17]. These results demonstrate that the proposed HTS method offers a compelling alternative for the synthesis of Cu SACs.

2.2. Structural Identification of Cu-N-C-HTS SAC

The as-synthesized Cu-N-C-HTS catalysts were initially examined using a combination of X-ray diffraction (XRD) and scanning electron microscopy (SEM). As shown in Fig. S8, the XRD patterns of all Cu-N-C-HTS samples present only a double peak corresponding to a low-crystallinity graphitic structure [40-42]. The absence of Cu reflections in the XRD profiles indicates a high dispersion of Cu species on the N-C support, which is further corroborated by the absence of Cu particles in the SEM images (Fig. S9-10). Furthermore, the Cu-N-C-HTS catalyst with the highest mass loading (0.54 wt%) was selected for further structural analysis. Transmission electron microscopy (TEM), scanning transmission electron microscopy (STEM), and N_2 adsorption-desorption isotherms were used to characterize the structure (Fig. 3(a) and Fig. S11-12). The Cu-N-C-HTS catalysts with different copper loadings show nitrogen adsorption-desorption isotherms and pore size distributions that are very similar to those of N-C, confirming the excellent structural stability of the carbon substrate, even after calcination at a high temperature of 1700 K [41].

Energy-dispersive X-ray spectroscopy (EDS) elemental maps (Fig. 3(b)) revealed that the three constituent elements, Cu, C, and N, are uniformly distributed throughout the nitrogen-doped carbon matrix. The Cu species trapped during HTS synthesis were further identified as isolated, single-atom dispersions using aberration-corrected high-angle annular dark-field scanning transmission electron microscopy (HAADF-STEM) (Fig. 3(c)). Moreover, the single cationic state of Cu, rather than metallic components, was confirmed by X-ray photoelectron spectroscopy (XPS). As shown in Fig. 3(d), the deconvoluted Cu 2p spectrum displays two sets of peaks with binding energies at 932.6/925.4 eV and

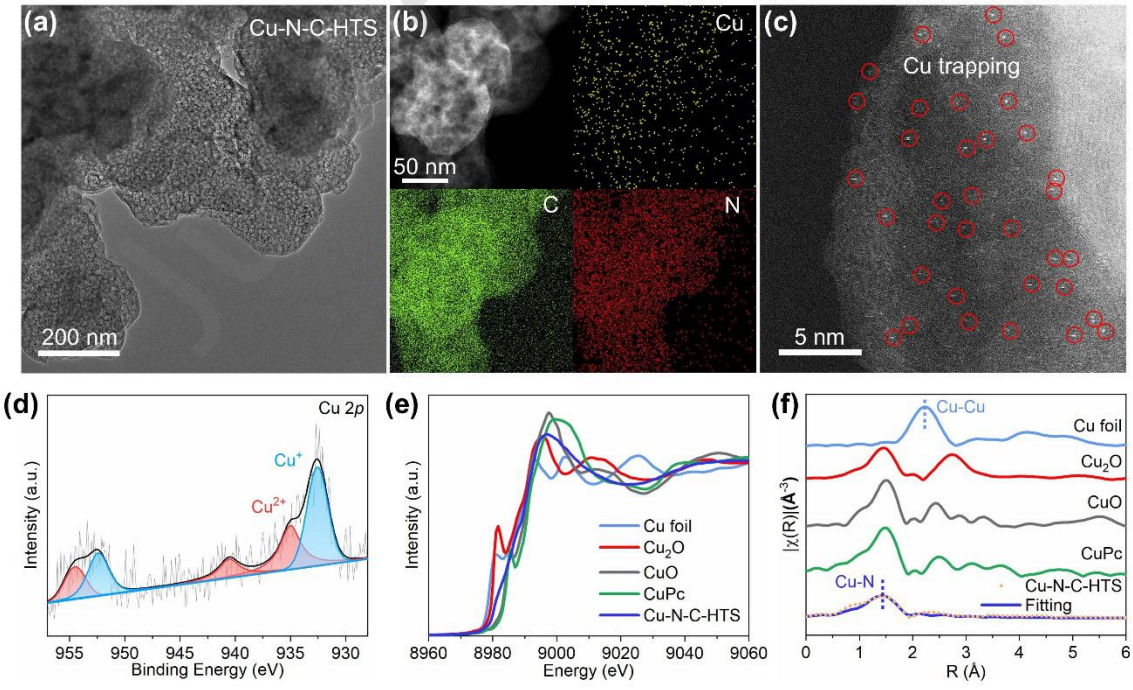

Figure 3. The structural information of Cu-N-C-HTS catalyst. (a) TEM image. (b) STEM image and corresponding elemental mapping including Cu/C/N. (c) HAADF-STEM image. (d) High-resolution Cu2p XPS spectra. (e) Cu K-edge XANES spectra of Cu-N-C-HTS and standard samples of Cu foil, Cu_2O, CuO and CuPc. (f) K^2-weighted (k) function of EXAFS spectra and the corresponding fitting curve.

935.0/954.5 eV, respectively, which can be attributed to Cu^{+}/Cu^{2+} species, along with a satellite peak for Cu^{2+} at 940.6 eV [43]. The detected Cu atomic content is 0.11 at%, corresponding to 0.57 wt%, which is consistent with the result from ICP analysis. Additionally, as shown in Fig. S13, the N 1s spectrum of Cu-N-C-HTS was deconvoluted into five components representing the pyridinic-N, pyridinic-N ligated Cu moiety, pyrrolic-N, graphitic-N, and oxidized-N [44]. Compared to untreated N-C, the Cu-N-C-HTS sample exhibits a significant increase in graphitic-N, along with a decrease in pyridinic-N species (Table S2), suggesting that carbothermal reduction induced graphitization, even with transient operation, which is consistent with the Raman results.

The single oxidized chemical state and local coordination environment of Cu-N-C-HTS were further corroborated using X-ray absorption near-edge spectroscopy (XANES) and extended X-ray absorption fine structure (EXAFS). The Cu K-edge XANES profiles of Cu-N-C-HTS, along with reference samples including Cu foil, Cu_2O, CuO, and copper phthalocyanine (CuPc), are shown in Fig. 3(e). The XANES edge profile of Cu-N-C-HTS falls between the profiles of divalent CuPc/CuO and monovalent Cu_2O, implying the presence of both Cu^{+} and Cu^{2+} species, consistent with the XPS results [45-47]. Fig. 3(f) presents the Fourier-transformed k^2-weighted EXAFS spectra at the Cu K-edge. Compared to the reference samples (Cu foil, Cu_2O, and CuO), the Cu-N-C-HTS catalyst lacks prominent peaks corresponding to Cu-Cu or Cu-O coordination, strongly suggesting the absence of metallic Cu or CuO/Cu_2O structures in the HTS-treated catalyst. However, the prominent peak at 1.48 Å (without phase correction) resembles the Cu-N distance in the CuPc reference, indicating that the active Cu atoms were trapped by defective nitrogen in the Cu-N-C-HTS catalyst. Furthermore, the best-fitting results of the EXAFS data (Table S3 and Fig. S14) show that the coordination number (CN) of the Cu-N shell is approximately 4 (actually 3.5), with a bond distance of 1.95 Å, corroborating the formation of a four-fold Cu-N coordination structure ($Cu\text{-}N_4$).

2.3. Reuse of Bulk Metal and Generality of HTS Synthesis

The recyclability of bulk metal is crucial for the scalable production of catalysts using HTS synthesis. As a proof-of-concept demonstration, Fig. 4(a) shows the successive reuse of Cu foil for the large-scale synthesis of Cu-N-C-HTS material. After 20 repeated HTS heating cycles, approximately 50 mg of Cu-N-C-HTS was obtained, with an average mass loading of 0.37 wt%. Macroscopically, the spent Cu foil remained glossy and flat without any deformation (as shown in Fig. 4(a)),

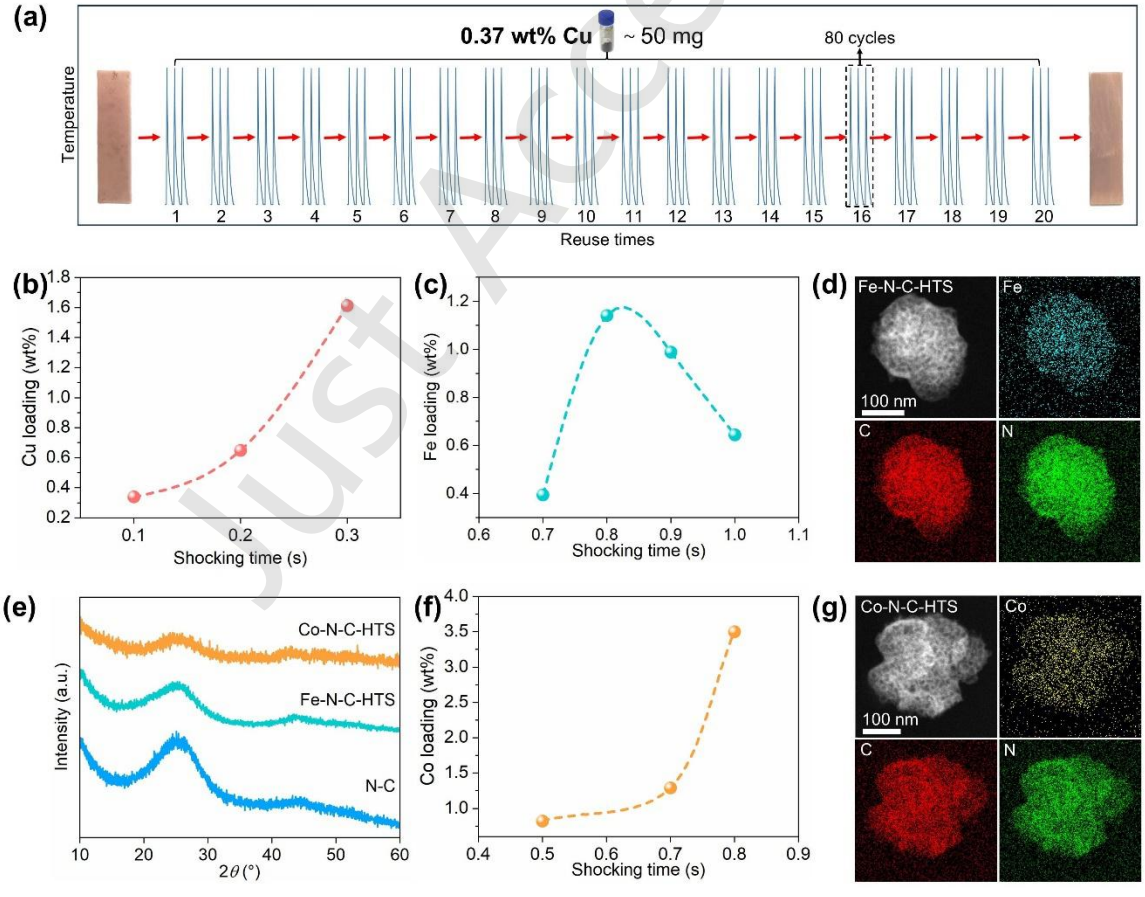

Figure 4. Generality of HTS synthesis for the highly dispersed metal catalysts. (a) Successive 20 times reuse of Cu foil for the Cu-N-C-HTS HTS synthesis. (b) Shocking time-dependent Cu mass weight of Cu-N-C-HTS-foam. (c) Shocking time-dependent Fe loading. (d) STEM image and corresponding EDS mapping of a highly dispersed metal region in Fe-N-C-HTS. (e) XRD patterns

of Fe-N-C-HTS and Co-N-C-HTS. (f) Shocking time-dependent Co loading. (g) STEM image and corresponding EDS mapping of a highly dispersed metal region in Co-N-C-HTS.

indicating the persistence of its textural characteristics during the HTS process. Fig. S15 also compares the XRD patterns of Cu foils before and after HTS processing. The (111) and (220) crystal planes are retained after successive heating pulses. However, the intensity of the (111) peak decreases due to the destruction of its unstable structure during HTS, indicating that the crystal structure plays a key role in Cu capture and the formation of Cu-N-C-HTS catalysts, which is further supported by subsequent theoretical calculations. Additionally, the surface energy of the (200) plane is higher than that of the (111) plane, resulting in lower thermodynamic stability during high-temperature treatment, leading to significant degradation or even disappearance of the (200) peak after HTS processing (Fig. S16) [48-50]. Besides, the XRD pattern of Cu-N-C-HTS-reuse aligns with that of N-C support, further evidencing the highly dispersed Cu species in as-prepared material (Fig. S17). It is also important to note that the scalability of catalyst yield in our home-built setup is limited by the size of the heating equipment (20 mm length and 5 mm width). In addition to the Cu foil, Cu foam can also serve as a metal precursor to produce the Cu-N-C-HTS sample. As shown in Fig. 4(b), after HTS treatment under operating conditions of 1700 K and 80 cycles, the Cu loading increased from 0.34 wt% to 0.65 wt% and then to 1.61 wt% for pulse times of 0.1, 0.2, and 0.3 s, respectively. The highest Cu loading of 1.61 wt% is almost eightfold higher than that of Cu foil under the same conditions. This sharp contrast is due to the open channels in the polyfoam, which act as chambers to increase the deposition surface of N-C. The XRD patterns did not show any Cu reflection peaks (Fig. S18), indicating that the trapped Cu species from the foam is highly dispersed on the nitrogen-doped carbon support. Furthermore, as displayed in Fig. S19, the STEM image and corresponding EDS mapping demonstrate the homogeneous distribution of Cu, C, and N throughout the open carbon structure without noticeable elemental segregation.

In addition to Cu-N-C-HTS material, the HTS strategy for the synthesis of highly dispersed metal catalysts demonstrates its generality, which can be extended to other transition metals, such as Fe and Co. Fig. 4(c) shows a volcano distribution of Fe loading with varying shock times from 0.7 to 1.0 s, reaching a maximum of 1.14 wt% at 0.8 s. Prolonged heating durations of 0.9 and 1.0 s led to a reduction in Fe loading, which can be partially attributed to the melting of the Fe foil. Relevant loading data can be found in Table S4. The STEM images of Fe-N-C-HTS and the corresponding elemental distribution map are shown in Fig. 4(d), which demonstrate that Fe, C, and N are evenly distributed on the support surface in regions without metal particles. This confirms the highly dispersed state of Fe species on the support. The XRD patterns of Fe-N-C-HTS catalysts with the highest metal mass loading were analyzed and showed characteristic peaks of low-graphitic carbon, which matched well with that of the raw N-C sample (Fig. 4(e)). This confirms the formation of highly dispersed Fe and Co species from each foil precursor. Fig. 4(f) shows that the mass weight of Co increased in a nearly linear fashion with shock time. Similarly, the STEM images of Co-N-C-HTS and the corresponding elemental distribution map show that Co, C, and N are evenly distributed on the support surface in regions without metal particles, confirming the highly dispersed state of Co species on the support (Fig. 4(g)). Due to the limited maximum current (39A) of the HTS power supply used in this study, which requires 0.5s to achieve a peak temperature of 1700 K, the relatively longer heating time may lead to aggregation of metal species and formation of particles in the catalyst (Fig. S20). Using a power supply with a higher current, enabling millisecond-scale heating and exceeding 2000 K, would allow for more controlled synthesis of highly dispersed metal catalysts [51].

2.4. Theoretical calculation

To better understand the synthetic mechanism from a theoretical perspective, we carried out *ab initio* molecular dynamics (AIMD) simulations to model the structural

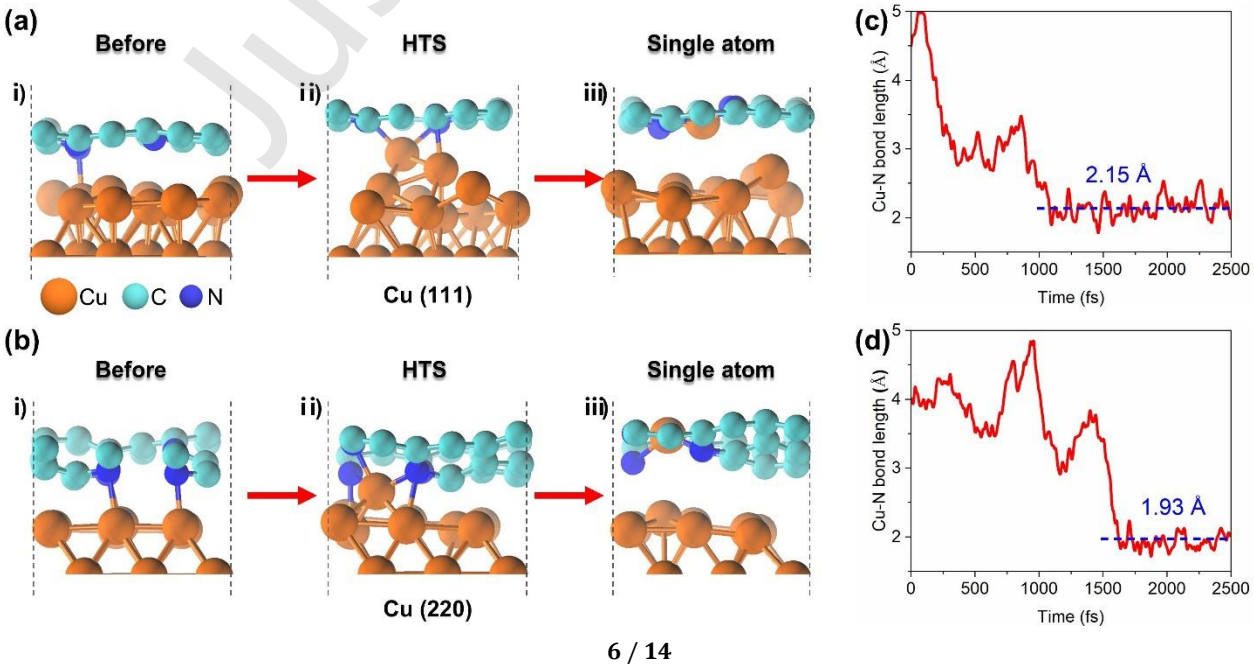

Figure 5. AIMD simulation analysis. (a) Side view of N-C/Cu (111) structure before/during/after HTS. (b) Side view of N-C/Cu (220) structure before/during/after HTS. (c) The bond length evolution of Cu-N in NG/Cu (111). (d) The bond length evolution of Cu-N in NG/Cu (220) during the AIMD simulation at 1300 K within 2.5 ps.

evolution from Cu foil to single atoms (Fig. S21). The theoretical structure corresponding to NC/Cu foil was modeled by assembling nitrogen-doped graphene (NG) on a Cu substrate (denoted as NG/Cu), where the two detected (111) and (220) planes in XRD were considered due to their persistence during HTS. The Cu (200) plane was not included in the calculations because of its intolerance to thermal treatment, as evidenced in Fig. 4(c). AIMD analysis reveals that, before HTS, a weak Cu-N interaction occurs between the NG and Cu substrate, without any significant structural deformation (Fig. 5(a-b)). The coordination between N and Cu atoms is insufficient to strip the bulk Cu precursor without further thermal activation. During HTS, the surface Cu atoms on both Cu (111) and Cu (220) planes are excited and vibrate dramatically, and the Cu atoms furthest from their equilibrium positions react with at least two nitrogen ligands. This indicates that the elevated temperature provides sufficient activation energy to make the metal atoms more reactive.

After HTS, Cu-N-C-HTS SAC is produced by forming thermodynamically stable Cu-N bonds. We also found that the Cu (220) plane could revert to its original state after HTS, whereas clusters formed on the Cu (111) surface showed irreversible structural distortion. The deformation of Cu (111) after HTS suggests structural degradation during prolonged thermal operation, which is also supported by XRD analysis showing attenuation in the peak intensity of Cu (111) after HTS (Fig. 4(c)). We also explored the evolution of the Cu-N bond length. As shown in Fig. 5(c-d), the Cu-N distance decreased significantly and then stabilized. The final bond lengths, measured at 2.15 Å and 1.93 Å for NG/Cu (111) and NG/Cu (220), respectively, agree with previously reported Cu-N bond lengths, indicating the successful synthesis of Cu-N-C-HTS SAC during HTS [52-53].

2.5. Activity Evaluation toward Ammonia Electrosynthesis

To demonstrate the functional applications of the HTS-produced Cu single atoms, we conducted electrocatalytic studies on NH_3 electrosynthesis via nitrite reduction, using N-C alone as a control [54-56]. The NH_3 product was quantified using the indophenol blue spectrophotometric method (calibration curve for NH_3 is shown in Fig. S22). The linear sweep voltammetry (LSV) polarization curves of the N-C and Cu-N-C-HTS catalysts are presented in Fig. 6(a). The Cu-N-C-HTS SAC exhibited a positive onset potential and significantly higher current density compared to the N-C support, with values of -0.03 V vs. RHE and -78.7 mA/cm^2 at -1.0 V vs. RHE, respectively. This comparison highlights the critical role of Cu active sites in transforming nitrite into NH_3.

We also quantified the NH_3 production rate, as shown in Fig. 6(b). The performance increased with increasingly negative potentials from -0.4 to -1.2 V vs. RHE, with a 6.5-fold improvement from 1.71 to 11.12 mg cm^{-2} h^{-1}. In contrast, the N-C support generated a much lower production rate of only 0.11 mg cm^{-2} h^{-1} under the same conditions. The related NH_3 Faradaic efficiency (FE) is shown in Fig. 6(c), indicating that the HTS-produced Cu SAC achieves high FE values exceeding 90% across the entire working potential window. This result strongly suggests the highly efficient conversion of nitrite to NH_3 on Cu single atoms, outperforming previously reported copper-based NO_2RR catalysts (Fig. 6(d) and Table S5). In comparison, the N-C catalyst exhibited a volcano-shaped FE profile and reached a lower FE of 17.85% at -0.8 V vs. RHE, significantly lower than that of the Cu-N-C-HTS catalyst. In addition to its excellent NO_2RR activity, Cu-N-C-HTS also exhibits outstanding electrocatalytic stability. As shown in Fig. S23, the catalyst demonstrates stable NH_3 production and FE_{NH3} over 10 consecutive cycles, with no significant

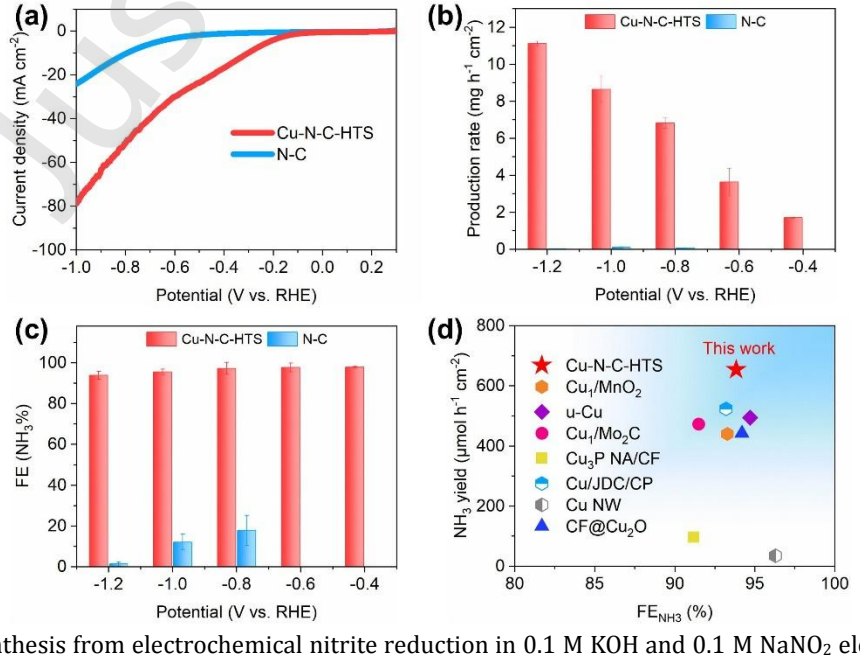

Figure 6. Ammonia synthesis from electrochemical nitrite reduction in 0.1 M KOH and 0.1 M $NaNO_2$ electrolytes. (a) The linear

sweep voltammetry (LSV) polarization curves of N-C and Cu-N-C-HTS catalysts. Production rate (b) and FE (c) of ammonia over Cu-N-C-HTS and N-C catalysts at different potentials. (d) NO_2RR performance comparison between Cu-N-C-HTS and recently reported Cu-based catalysts.60-66

decrease in current density during the test, indicating the excellent cycling durability of Cu-N-C-HTS. Furthermore, after the stability test, HAADF-STEM images of the catalyst show that some copper atoms have formed clusters and a significant portion of copper single atoms remains. EDS mapping reveals that copper species are uniformly distributed on the support surface, confirming that Cu-N-C-HTS can partially retain its single-atom Cu coordination and content, which indicates its structural stability (Fig. S24). In situ FTIR analysis further identifies the intermediates formed during the NO_2RR electrolysis on Cu-N-C-HTS (Fig. S25), confirming that Cu-N-C-HTS follows the NHO pathway to drive the NO_2RR process, with the specific pathway being $*NO_2 \rightarrow *NO \rightarrow *NH_2OH \rightarrow *NH_2 \rightarrow *NH_3$ [57-59].

3 Conclusion

In this work, we developed an ultrafast synthesis method using high-temperature shock (HTS) to produce single atoms directly from bulk copper metal and demonstrated its applicability for other metal-supported catalysts. This HTS approach is enabled by electrical heating over a few seconds, providing high temperatures for short durations. The Cu-N-C-HTS catalyst was synthesized from Cu foil subjected to a heating shock for just 0.5 seconds at 1700 K. Structural characterizations in the combination of XAFS and HADDF-STEM identify the single-atom dispersion of Cu speciation within local $Cu-N_4$ configuration. Theoretical calculations using AIMD simulation further revealed that the transient high temperature provides sufficient dynamic energy to make Cu atoms more reactive, thus facilitating the formation of thermodynamically favorable Cu-N bonds. The HTS-produced Cu single atoms exhibited excellent catalytic activity for ammonia synthesis from a nitrite precursor, achieving a FE of 90% and an NH_3 production rate of 11.12 mg cm^{-2} h^{-1} at -1.2 V vs. RHE, outperforming previously reported Cu-based nitrite reduction electrocatalysts. In addition to using Cu foil, other metal precursors such as Fe and Co foils and Cu foam were subjected to HTS, with structural analyses indicating that these metal species can also be supported on the substrate. In summary, the proposed HTS strategy is simple and amenable to the large-scale production of SACs from bulk metal for industrial applications.

4 Method

4.1 Materials

NaOH (96%, TianDa Chemical Reagent), 2,6-diaminopyridine (98%, Aladdin), ammonium persulfate (98%, Aladdin), Ludox colloidal silica (40wt% in water, Sigma-Aldrich), ethanol (99.7%, Tianjin Fuyu), copper nitrate hydrate (99%, DaMao) and ultra-pure water (resistivity of 18.2 MΩ·cm) were purchased for the preparation of Cu-N-C catalyst. KOH (90%, Sigma-Aldrich), KNO_3 (99.99%, Aladdin), glassy-carbon electrode were purchased for electrochemical tests. Sodium hypochlorite solution (6-14% active chlorine, Aladdin), Sodium salicylate (99.5%, Damao), Sodium nitroferricyanide dehydrate (99%, Aladdin) and NaOH (96%, Aladdin) were used for the ammonia quantitation. Hydrochloric acid (AR), sulfuric acid (AR), and ethyl alcohol (AR) were purchased from Sinopharm Chemical Reagent Co., Ltd. Nafion (5%) was purchased from Du Pont China Holding Co., Ltd. Carbon cloth (CC) and conductive carbon paper were purchased from Ce Tech Co., Ltd.

4.2 Synthesis of N-C

The nitrogen/carbon precursor was initially synthesized through a chemical oxidation process. In this process, 3 mL of 40% colloidal silica was mixed with 5.45 g of 2,6-diaminopyridine and ultrasonically dispersed in 400 mL of water. Subsequently, 1 g of NaOH was added to the mixture and stirred for an additional 10 minutes to ensure complete dissolution. Following this, the mixed solution was subjected to chemical oxidation by the gradual addition of an $(NH_4)_2S_2O_8$ aqueous solution (18.57 g/100 mL) under vigorous stirring in an ice bath for 12 hours. The resulting product was collected via filtration and dried at 80 °C overnight. To prepare the N-C support, the dried material underwent pyrolysis at 800 °C for 2 hours under a flow of NH_3/Ar stream and was then allowed to cool naturally to room temperature, resulting in SiO_2@N-C. Finally, the silica was acid-leached using a 10% HF solution for 4 hours, leaving behind the porous nitrogen-doped carbon, referred to as N-C.

4.3 Cu-N-C-HTS synthesized by high-temperature shock

Firstly, 50 mg of N-C catalyst support was dispersed in 1 mL of ethanol and ultrasonicated for 0.5 hours to prepare a 50 mg mL^{-1} carrier solution. Subsequently, 50 μL of this solution was uniformly applied onto a Cu foil (20×5×0.2 mm) that had been abraded with sandpaper to remove the oxide layer and cleaned with ethanol. The foil was then left to air dry. The Cu foil coated with N-C immobilized into two layers of carbon cloth (CC, 60×10 mm) was placed into a homemade carbon heater in N_2, and the two sides of the CC were connected with a Cu electrode. The output electric current, discharge time and the number of repetitions were regulated using a DC power supply. In a typical heating program, the electrical power applied to the carbon heater was switched from the 'off' state to the 'on' state and held for 0.5 s to carry out the carbothermal reduction, followed by removing the power to turn the heater back off for 5 s to complete a period of 5.5 s, which is then repeated 80 cycles to synthesize the Cu-N-C-HTS. After synthesis, the solid product on the surface of the Cu foil was collected, and the foil, once cleaned, was reused for subsequent syntheses. Copper foil can be expanded to copper foam or other metal foil to synthesize M-N-C.

4.4 Materials characterization

The infrared pyrometer (IMPAC IMGA 740) was applied for noncontact temperature measurement during the pulse heating. The powder XRD was performed on an X-ray diffractometer (Rigaku, Ultima-IV) with a Cu Kα radiation source (scanning speed, 10°min^{-1}). The XPS spectra were obtained on an X-ray photoelectron spectrometer (Thermo Scientific ESCALAB Xi+). The metal content of catalysts was measured by ICP-OES (SPECTRO SPECTROBLUE FMX36). SEM images were obtained on a field emission scanning electron microscopy and EDX elemental mapping analysis (Zeiss GeminiSEM 500). Raman spectra were acquired by a Renishaw inVia confocal microscope Raman system, with 532 nm laser as the excitation source. The morphologies and microstructures of the prepared catalysts were determined by a JEOL JEM-F200 STEM/TEM system. Nitrogen adsorption/desorption isotherms were obtained using on a Micromeritics ASAP 2460 apparatus (Quadrasorb SI Automate Surface Area & Pore Size Analyzer) at -196 °C, and specific surface areas were calculated based on the Brunauer-Emmett-Teller (BET) method. The atomic copper species were observed on a JEOL JEM-ARM200F STEM/TEM by dropping the diluted catalyst on copper mesh grid. The

XAS spectra containing XANES and EXAFS at the Cu K-edge were collected at the BL14W of Shanghai Synchrotron Radiation Facility (SSRF), Shanghai Institute of Applied Physics (SINAP), China.

4.5 Electrochemical measurements

Electrochemical experiments were conducted using a CHI 660 instrument, which was equipped with a sealed H-type cell separated by a proton exchange membrane (Nafion-117). A silver/silver chloride (Ag/AgCl) electrode with a salt bridge served as the reference electrode, while a platinum foil (1*1 cm^2) was used as the counter electrode. For the preparation of the catalyst ink, 5 mg of catalyst powder was dispersed in a mixture of 10 μL of 5 wt% Nafion solution, 500 μL H_2O and 490 uL ethanol, followed by sonication for 30 minutes. The resulting well-dispersed catalyst ink was then uniformly applied onto a glass-carbon substrate with an area of 0.196 cm^2 and dried at a room temperature. For electrochemical nitrite reduction, an Ar-saturated solution of 0.1 M KOH containing 0.1 M $NaNO_2$ was used as the electrolyte. Nitrite polarization was assessed using linear sweep voltammetry (LSV) at a scan rate of 10 mV s^{-1} over a potential range of 0.25 to -1.2 V vs. RHE. Chronoamperometric tests were carried out at various potentials (-0.40, -0.60, -0.80, -1.00, -1.2 V vs. RHE) for 30 minutes. All applied potentials were calibrated against the reversible hydrogen electrode (RHE) using the equation:

$$E_{RHE} = E_{Ag/AgCl} + 0.059 * pH + 0.197\ V.$$

4.5 Product quantification by IBS

Ammonia: The quantification of ammonia was performed using the indophenol blue spectrophotometric (IBS) method. The chromogenic agents were prepared as follows:

Solution C#: 1 g of sodium nitroferricyanide dihydrate was dissolved in 100 mL of water.

Solution A#: 6.404 g of sodium salicylate and 1.312 g of NaOH were dissolved in 100 mL of water.

Solution B#: 7.5 mL of sodium hypochlorite solution and 3.075 g of NaOH were dissolved in 100 mL of water.

A specific volume of the reaction electrolyte was extracted and diluted with 0.1 M KOH to a final volume of 4 mL. Subsequently, 320 μL of Solution C# was added, followed by 2.4 mL of Solution A# and 800 μL of Solution B#. The absorbance of ammonia was measured in the wavelength range of 500 to 800 nm using an ultraviolet-visible (UV-Vis) spectrophotometer. The ammonia concentration was then determined using a standard calibration curve.

4.6 Faradaic efficiency

The selectivity for ammonia product can be calculated using the following equation:

$$Faradaic\ efficiency\ (\%) = (n_E \cdot F \cdot 100\%)/Q_T$$

where:

n_e represents the number of moles of electrons required for the production of ammonia (6 e^-),

F is the Faraday constant (96485 C mol^{-1}),

Q_T is the total charge passed through the electrode,

n denotes the moles of ammonia or nitrite produced, and

t refers to the duration of the electrolysis.

4.7 Computational methods

In present work, all density functional theory (DFT) with spin polarization calculations were implemented in the Vienna Ab Initio Simulation Package (VASP) code. The Perdew-Burke-Ernzerhof (PBE) functional within the generalized gradient approximation (GGA) was adopted to describe electronic exchange-correlation energy. The ionic cores were described with the projector augmented wave (PAW) method. The calculated NG/Cu (111) and NG/Cu (220) structures were the periodic boundary conditions in x- and y-direction. And in the z-directions, the structure was separated by 15 Å vacuum height from its neighbours. A basis set of plane waves was up to an energy cutoff of 450 eV. The localized d electrons correlation for Fe metal can be described by DFT + U method, and the van der Waals interaction between NG and Cu slabs are described via DFT-D3 correlation. For the structure optimization and energy calculations, the K-points were set to be 2 × 2 ×1. All of the calculations were continued until the force and energy have converged to less than 0.02 eV $Å^{-1}$ and 10^{-5} eV, respectively. The AIMD simulations were performed using canonical ensemble (NVT) and Nosé-Hoover thermostat method at 1300 K and lasted for 5 ps with a time step of 1 fs. Longer simulation times were not used, as the total energy of all systems had reached equilibrium within 2 ps.

Data availability

All data needed to support the conclusions in the paper are presented in the manuscript and/or the Electronic Supplementary Material. Additional data related to this paper may be requested from the corresponding author upon request."

Acknowledgements

The authors acknowledge financial support from the National Natural Science Foundation of China (22222305, 22402164 and 22021001), the Fundamental Research Funds for the Central Universities (20720220013).

Declaration of competing interest

All the contributing author(s) report(s) no conflict of interests in this work.

Author contribution statement

Renjie Fang and Ji Yang: Data curation, project administration, validation, writing manuscript, experimental design. Wei-Shen Song, Na Yang and Jie Ding: Data curation. Ji Yang, Jian-Feng Li and Feng Ru Fan: Project administration, funding acquisition, writing manuscript. All the authors have approved the final manuscript.

Informed consent

Not applicable.

Ethics statement

Not applicable.

Use of AI statement

None.

References

[1] Qiao, B. T.; Wang, A. Q.; Yang, X. F.; Allard, L. F.; Jiang, Z.; Cui, Y. T.; Liu, J. Y.; Li, J.; Zhang, T. Single-atom catalysis of CO oxidation using Pt_1/FeO_x. *Nat Chem* **2011**, 3, 634.

[2] Yang, X. F.; Wang, A. Q.; Qiao, B. T.; Li, J.; Liu, J. Y.; Zhang, T. Single-Atom Catalysts: A New Frontier in Heterogeneous Catalysis. *Accounts Chem Res* **2013**, 46, 1740.

[3] Wang, A. Q.; Li, J.; Zhang, T. Heterogeneous single-atom catalysis. *Nat Rev Chem* **2018**, 2, 65.

[4] Chen, Y. J.; Ji, S. F.; Chen, C.; Peng, Q.; Wang, D. S.; Li, Y. D. Single-Atom Catalysts: Synthetic Strategies and Electrochemical Applications. *Joule* **2018**, 2, 1242.

[5] Han, L. L.; Cheng, H.; Liu, W.; Li, H. Q.; Ou, P. F.; Lin, R. Q.; Wang, H. T.; Pao, C. W.; Head, A. R.; Wang, C. H.; et al. A single-atom library for guided monometallic and concentration-complex

multimetallic designs. *Nat Mater* **2022**, 21, 681.

[6] Rong, H. P.; Ji, S. F.; Zhang, J. T.; Wang, D. S.; Li, Y. D. Synthetic strategies of supported atomic clusters for heterogeneous catalysis. *Nat Commun* **2020**, 11, 5884.

[7] Wang, Y.; Wang, D. S.; Li, Y. D. Rational Design of Single-Atom Site Electrocatalysts: From Theoretical Understandings to Practical Applications. *Adv Mater* **2021**, 33, 2008151.

[8] Huang, Y.; Chen, Y. C.; Xu, M. J.; Ly, A.; Gili, A.; Murphy, E.; Asset, T.; Liu, Y. C.; De Andrade, V.; Segre, C. U.; et al. Catalysts by pyrolysis: Transforming metal-organic frameworks (MOFs) precursors into metal-nitrogen-carbon (M-N-C) materials. *Mater Today* **2023**, 69, 66.

[9] Li, J. Z.; Chen, M. J.; Cullen, D. A.; Hwang, S.; Wang, M. Y.; Li, B. Y.; Liu, K. X.; Karakalos, S.; Lucero, M.; Zhang, H. G.; et al. Atomically dispersed manganese catalysts for oxygen reduction in proton-exchange membrane fuel cells. *Nat Catal* **2018**, 1, 935.

[10] Liang, H. W.; Brüller, S.; Dong, R. H.; Zhang, J.; Feng, X. L.; Müllen, K. Molecular metal-N_x centres in porous carbon for electrocatalytic hydrogen evolution. *Nat Commun* **2015**, 6, 7992.

[11] Zitolo, A.; Goellner, V.; Armel, V.; Sougrati, M. T.; Mineva, T.; Stievano, L.; Fonda, E.; Jaouen, F. Identification of catalytic sites for oxygen reduction in iron- and nitrogen-doped graphene materials. *Nat Mater* **2015**, 14, 937.

[12] He, Y. H.; Shi, Q. R.; Shan, W. T.; Li, X.; Kropf, A. J.; Wegener, E. C.; Wright, J.; Karakalos, S.; Su, D.; Cullen, D. A.; et al. Dynamically Unveiling Metal-Nitrogen Coordination during Thermal Activation to Design High-Efficient Atomically Dispersed CoN_4 Active Sites. *Angew Chem Int Edit* **2021**, 60, 9516.

[13] Li, J. Z.; Zhang, H. G.; Samarakoon, W.; Shan, W. T.; Cullen, D. A.; Karakalos, S.; Chen, M. J.; Gu, D. M.; More, K. L.; Wang, G. F.; et al. Thermally Driven Structure and Performance Evolution of Atomically Dispersed FeN_4 Sites for Oxygen Reduction. *Angew Chem Int Edit* **2019**, 58, 18971.

[14] Qu, Y.; Chen, B.; Li, Z.; Duan, X.; Wang, L.; Lin, Y.; Yuan, T.; Zhou, F.; Hu, Y.; Yang, Z.; et al. Thermal Emitting Strategy to Synthesize Atomically Dispersed Pt Metal Sites from Bulk Pt Metal. *J Am Chem Soc* **2019**, 141, 4505.

[15] Li, Y.; Wang, S.; Wang, X.-S.; He, Y.; Wang, Q.; Li, Y.; Li, M.; Yang, G.; Yi, J.; Lin, H.; et al. Facile Top-Down Strategy for Direct Metal Atomization and Coordination Achieving a High Turnover Number in CO_2 Photoreduction. *J Am Chem Soc* **2020**, 142, 19259.

[16] Jones, J.; Xiong, H.; DeLaRiva, A. T.; Peterson, E. J.; Hien, P.; Challa, S. R.; Qi, G.; Oh, S.; Wiebenga, M. H.; Hernandez, X. I. P.; et al. Thermally stable single-atom platinum-on-ceria catalysts via atom trapping. *Science* **2016**, 353, 150.

[17] Yang, Z. K.; Chen, B. X.; Chen, W. X.; Qu, Y. T.; Zhou, F. Y.; Zhao, C. M.; Xu, Q.; Zhang, Q. H.; Duan, X. Z.; Wu, Y. Directly transforming copper (I) oxide bulk into isolated single-atom copper sites catalyst through gas-transport approach. *Nat Commun* **2019**, 10, 3734.

[18] Qu, Y. T.; Li, Z. J.; Chen, W. X.; Lin, Y.; Yuan, T. W.; Yang, Z. K.; Zhao, C. M.; Wang, J.; Zhao, C.; Wang, X.; et al. Direct transformation of bulk copper into copper single sites via emitting and trapping of atoms. *Nat Catal* **2018**, 1, 781.

[19] Fan, Y. M.; Li, R. T.; Wang, B. B.; Feng, X. H.; Du, X. Z.; Liu, C. X.; Wang, F.; Liu, C. H.; Dong, C.; Ning, Y. X.; et al. Water-assisted oxidative redispersion of Cu particles through formation of Cu hydroxide at room temperature. *Nat Commun* **2024**, 15, 3046.

[20] Yang, J.; Qi, H. F.; Li, A. Q.; Liu, X. Y.; Yang, X. F.; Zhang, S. X.; Zhao, Q.; Jiang, Q. K.; Su, Y.; Zhang, L. L.; et al. Potential-Driven Restructuring of Cu Single Atoms to Nanoparticles for Boosting the Electrochemical Reduction of Nitrate to Ammonia. *J Am Chem Soc* **2022**, 144, 12062.

[21] Yao, Y.; Huang, Z.; Xie, P.; Lacey, S. D.; Jacob, R. J.; Xie, H.; Chen, F.; Nie, A.; Pu, T.; Rehwoldt, M.; et al. Carbothermal shock synthesis of high-entropy-alloy nanoparticles. *Science* **2018**, 359, 1489.

[22] Han, Y.-C.; Yi, J.; Pang, B.; Wang, N.; Li, X.-C.; Yao, T.; Novoselov, K. S.; Tian, Z.-Q. Graphene-confined ultrafast radiant heating for high-loading subnanometer metal cluster catalysts. *Natl Sci Rev* **2023**, 10, 6.

[23] Jiang, D.; Yao, Y. G.; Li, T. Y.; Wan, G.; Pereira-Hernández, X. I.; Lu, Y. B.; Tian, J. S.; Khivantsev, K.; Engelhard, M. H.; Sun, C. J.; et al. Tailoring the Local Environment of Platinum in Single-Atom Pt_1/CeO_2 Catalysts for Robust Low-Temperature CO Oxidation. *Angew Chem Int Edit* **2021**, 60, 26054.

[24] Huang, B.; Wang, M. H.; Wu, C. X.; Guan, L. H., Highly Dispersive Metal Atoms Anchored on Carbon Matrix Obtained by Direct Rapid Pyrolysis of Metal Complexes. *Ccs Chem* **2022**, 4 (9), 2968-2979.

[25] Lin, Y. X.; Wang, Y.; Xu, Y.; Liu, H. J.; Liu, X.; Shan, L.; Wu, C. Q.; Yang, L.; Song, L., Optimizing Local Configuration of Interphase Copper Oxide by Ru Atoms Incorporation for High-Efficient Nitrate Reduction to Ammonia. *Adv Funct Mater* **2024**, 2417486.

[26] Hu, X.; Zuo, D.; Cheng, S.; Chen, S.; Liu, Y.; Bao, W.; Deng, S.; Harris, S. J.; Wan, J. Ultrafast materials synthesis and manufacturing techniques for emerging energy and environmental applications. *Chem Soc Rev* **2023**, 52, 1103.

[27] Han, Y.-C.; Cao, P.-Y.; Tian, Z.-Q. Controllable Synthesis of Solid Catalysts by High-Temperature Pulse. *Accounts Mater Res* **2023**, 4, 648.

[28] Yao, Y.; Huang, Z.; Xie, P.; Wu, L.; Ma, L.; Li, T.; Pang, Z.; Jiao, M.; Liang, Z.; Gao, J.; et al. High temperature shockwave stabilized single atoms. *Nat Nanotechnol* **2019**, 14, 851.

[29] Xi, D. W.; Li, J. Y.; Low, J. X.; Mao, K. K.; Long, R.; Li, J. W.; Dai, Z. H.; Shao, T. Y.; Zhong, Y.; Li, Y.; et al. Limiting the Uncoordinated N Species in M-N_x Single-Atom Catalysts toward Electrocatalytic CO_2 Reduction in Broad Voltage Range. *Adv Mater* **2022**, 34, 2104090.

[30] Xing, L. L.; Liu, R.; Gong, Z. C.; Liu, J. J.; Liu, J. B.; Gong, H. S.; Huang, K.; Fei, H. L. Ultrafast Joule heating synthesis of hierarchically porous graphene-based Co-N-C single-atom monoliths. *Nano Res* **2022**, 15, 3913.

[31] Du, J. Y.; Wu, G.; Liang, K.; Yang, J.; Zhang, Y. D.; Lin, Y.; Zheng, X. S.; Yu, Z. Q.; Wu, Y.; Hong, X. Rapid Controllable Synthesis of Atomically Dispersed Co on Carbon under High Voltage within One Minute. *Small* **2021**, 17, 2007264.

[32] Gong, H. S.; Wei, Z. X.; Gong, Z. C.; Liu, J. J.; Ye, G. L.; Yan, M. M.; Dong, J. C.; Allen, C.; Liu, J. B.; Huang, K.; et al. Low-Coordinated Co-N-C on Oxygenated Graphene for Efficient Electrocatalytic H_2O_2 Production. *Adv Funct Mater* **2022**, 32, 2106886.

[33] Yue, Y. X.; Wang, S. S.; Zhou, Q.; Wang, B. L.; Jin, C. X.; Chang, R. Q.; Wan, L. Q.; Pan, Z. Y.; Zhu, Y. H.; Zhao, J.; et al. Tailoring Asymmetric Cu-O-P Coupling Site by Carbothermal Shock Method for Efficient Vinyl Chloride Synthesis over Carbon Supported Cu Catalysts. *Acs Catal* **2023**, 13, 9777.

[34] Liu, K. Y.; Sun, Z. Y.; Chen, W. X.; Lang, X. F.; Gao, X.; Chen, P. W. Ultra-Fast Pulsed Discharge Preparation of Coordinatively Unsaturated Asymmetric Copper Single-Atom Catalysts for CO_2 Reduction. *Adv Funct Mater* **2024**, 34, 2312589.

[35] Dong, Q.; Lele, A. D.; Zhao, X. P.; Li, S. K.; Cheng, S. C.; Wang, Y. Q.; Cui, M. J.; Guo, M.; Brozena, A. H.; Lin, Y.; et al. Depolymerization of plastics by means of electrified spatiotemporal heating. *Nature* **2023**, 616, 488.

[36] Dong, Q.; Yao, Y. G.; Cheng, S. C.; Alexopoulos, K.; Gao, J. L.; Srinivas, S.; Wang, Y. F.; Pei, Y.; Zheng, C. L.; Brozena, A. H.; et al. Programmable heating and quenching for efficient thermochemical synthesis. *Nature* **2022**, 605, 470.

[37] Yao, Y. G.; Huang, Z. N.; Xie, P. F.; Lacey, S. D.; Jacob, R. J.; Xie, H.; Chen, F. J.; Nie, A. M.; Pu, T. C.; Rehwoldt, M.; et al. Carbothermal shock synthesis of high-entropy-alloy nanoparticles. *Science* **2018**, 359, 1489.

[38] Niu, W. J.; Sun, Q. Q.; He, J. Z.; Chen, J. L.; Gu, B. N.; Liu, M. J.; Chung, C. C.; Wu, Y. Z.; Chueh, Y. L., Zeolitic imidazolate framework-derived copper single atom anchored on nitrogen-doped porous carbon as a highly efficient electrocatalyst for the oxygen reduction reaction toward Zn-airbattery. *Chem Mater* **2022**, 34 (9), 4104-4114.

[39] Han, G. F.; Li, F.; Rykov, A. I.; Im, Y. K.; Yu, S. Y.; Jeon, J. P.; Kim, S. J.; Zhou, W. H.; Ge, R.; Ao, Z. M.; et al. Abrading bulk metal into single atoms. *Nat Nanotechnol* **2022**, 17, 403.

[40] Wang, Y. X.; Li, B. Y.; Xue, B.; Libretto, N.; Xie, Z. H.; Shen, H.; Wang, C. H.; Raciti, D.; Marinkovic, N.; Zong, H.; et al. CO electroreduction on single-atom copper. *Sci Adv* **2023**, 9, eade3557.

[41] Yang, J.; Liu, W. G.; Xu, M. Q.; Liu, X. Y.; Qi, H. F.; Zhang, L. L.; Yang, X. F.; Niu, S. S.; Zhou, D.; Liu, Y. F.; et al. Dynamic Behavior of Single-Atom Catalysts in Electrocatalysis: Identification of Cu-N_3 as an Active Site for the Oxygen Reduction Reaction. *J Am Chem Soc* **2021**, 143, 14530.

[42] Shang, H. S.; Zhou, X. Y.; Dong, J. C.; Li, A.; Zhao, X.; Liu, Q. H.; Lin, Y.; Pei, J. J.; Li, Z.; Jiang, Z. L.; et al. Engineering unsymmetrically coordinated Cu-S1N3 single atom sites with enhanced oxygen reduction activity. *Nat Commun* **2020**, 11, 3049.

[43] Sun, T. T.; Li, Y. L.; Cui, T. T.; Xu, L. B.; Wang, Y. G.; Chen, W. X.; Zhang, P. P.; Zheng, T. Y.; Fu, X. Z.; Zhang, S. L.; et al. Engineering of Coordination Environment and Multiscale Structure in Single-Site Copper Catalyst for Superior Electrocatalytic Oxygen Reduction. *Nano Lett* **2020**, 20, 6206.

[44] Lai, Q.; Zhu, J.; Zhao, Y.; Liang, Y.; He, J.; Chen, J. MOF-Based Metal-Doping-Induced Synthesis of Hierarchical Porous Cu-N/C Oxygen Reduction Electrocatalysts for Zn-Air Batteries. *Small* **2017**, 13, 1700740.

[45] Rehr, J. J.; Albers, R. C. Theoretical approaches to x-ray absorption fine structure. *Rev Mod Phys* **2000**, 72, 621.

[46] Bunau, O.; Joly, Y. Self-consistent aspects of x-ray absorption calculations. *J Phys-Condens Mat* **2009**, 21, 345501.

[47] Joly, Y. X-ray absorption near edge structure calculation beyond the muffin-tin approximation. *Journal De Physique Iv* **1997**, 7, 111.

[48] Da Silva, J. L. F.; Barreteau, C.; Schroeder, K.; Blügel, S., All-electron first-principles investigations of the energetics of vicinal Cu surfaces. *Phys Rev B* **2006**, 73 (12).

[49] Skriver, H. L.; Rosengaard, N. M., Surface energy and work function of elemental metals. *Phys Rev B* **1992**, 46 (11), 7157-7168.

[50] Vitos, L.; Skriver, H. L.; Kollár, J., The formation energy for steps and kinks on cubic transition metal surfaces. *Surf Sci* **1999**, 425 (2-3), 212-223.

[51] Deng, B.; Wang, Z.; Chen, W. Y.; Li, J. T. C.; Luong, D. X.; Carter, R. A.; Gao, G. H.; Yakobson, B.; Zhao, Y. F.; Tour, J. M., Phase controlled synthesis of transition metal carbide nanocrystals by ultrafast flash Joule heating. *Nat Commun* **2022**, 13 (1).

[52] Karapinar, D.; Huan, N. T.; Sahraie, N. R.; Li, J. K.; Wakerley, D.; Touati, N.; Zanna, S.; Taverna, D.; Tizei, L. H. G.; Zitolo, A.; et al. Electroreduction of CO_2 on Single-Site Copper-Nitrogen-Doped Carbon Material: Selective Formation of Ethanol and Reversible Restructuration of the Metal Sites. *Angew Chem Int Edit* **2019**, 58, 15098.

[53] Li, F.; Han, G. F.; Noh, H. J.; Kim, S. J.; Lu, Y. L.; Jeong, H. Y.; Fu, Z. P.; Baek, J. B. Boosting oxygen reduction catalysis with abundant copper single atom active sites. *Energ Environ Sci* **2018**, 11, 2263.

[54] Zhao, H. Y.; Xiang, J. Q.; Sun, Z. Y.; Shang, S. Y.; Chu, K. Electroreduction of Nitrite to Ammonia over a Cobalt Single-Atom Catalyst. *Acs Sustain Chem Eng* **2024**, 12, 2783.

[55] Xiang, J. Q.; Zhao, H. Y.; Chen, K.; Yang, X.; Chu, K. Electrocatalytic nitrite reduction to ammonia on an Rh single-atom catalyst. *J Colloid Interf Sci* **2024**, 659, 432.

[56] Jiang, Z.; Wang, Y. M.; Lin, Z. C.; Yuan, Y. B.; Zhang, X.; Tang, Y. R.; Wang, H. X.; Li, H.; Jin, C. Y.; Liang, Y. Y. Molecular electrocatalysts for rapid and selective reduction of nitrogenous waste to ammonia. *Energ Environ Sci* **2023**, 16, 2239.

[57] Wang, F. Z.; Zhao, H. Y.; Zhang, G. K.; Zhang, H.; Han, X. P.; Chu, K., Electroreduction of Nitrite to Ammonia Over Ni_1Ru Single-Atom Alloys. *Adv Funct Mater* **2024**, 34 (3).

[58] Xiang, J. Q.; Qiang, C. F.; Shang, S. Y.; Chen, K.; Kang, C. Y.; Chu, K., Tandem electrocatalytic reduction of nitrite to ammonia on rhodium-copper single atom alloys. *Adv Funct Mater* **2024**, 34 (36).

[59] Wang, F. Z.; Shang, S. Y.; Sun, Z. Y.; Yang, X.; Chu, K., P-block antimony-copper single-atom alloys for selective nitrite electroreduction to ammonia. *Acs Nano* **2024**, 18 (20), 13141-13149.

[60] Chen, Q. Y.; An, X. G.; Liu, Q.; Wu, X. Q.; Xie, L. S.; Zhang, J.; Yao, W. T.; Hamdy, M. S.; Kong, Q. Q.; Sun, X. P. Boosting electrochemical nitrite-ammonia conversion properties by a Cu foam@Cu_2O catalyst. *Chem Commun* **2022**, 58, 517.

[61] Liang, J.; Deng, B.; Liu, Q.; Wen, G. L.; Liu, Q.; Li, T. S.; Luo, Y. L.; Alshehri, A. A.; Alzahrani, K. A.; Ma, D. W.; et al. High-efficiency electrochemical nitrite reduction to ammonium using a Cu_3P nanowire array under ambient conditions. *Green Chem* **2021**, 23, 5487.

[62] Ouyang, L.; Yue, L. C.; Liu, Q.; Liu, Q.; Li, Z. R.; Sun, S. J.; Luo, Y. S.; Alshehri, A. A.; Hamdy, M. S.; Kong, Q. Q.; et al. Cu nanoparticles decorated juncus-derived carbon for efficient electrocatalytic nitrite-to-ammonia conversion. *J Colloid Interf Sci* **2022**, 624, 394.

[63] Wan, Y. Y.; Du, W. Y.; Chen, K.; Zhang, N. A.; Chu, K. Electrocatalytic nitrite-to-ammonia reduction on isolated Cu sites. *J Colloid Interf Sci* **2023**, 652, 2180.

[64] Wang, G. H.; Ma, R. Y.; Zhang, N. A.; Guo, Y. L.; Chu, K. Single-atom Cu anchored on Mo_2C boosts nitrite electroreduction to ammonia. *Chem Commun* **2023**, 59, 13887.

[65] Zhang, R. C.; Shang, S. Y.; Wang, F. Z.; Chu, K. Electrocatalytic reduction of nitrite to ammonia on undercoordinated Cu. *Dalton T* **2024**, 53, 3470.

[66] Zhang, Y. Y.; Wang, Y.; Han, L.; Wang, S. N.; Cui, T. D.; Yan, Y. F.; Xu, M.; Duan, H. H.; Kuang, Y.; Sun, X. M. Nitrite Electroreduction to Ammonia Promoted by Molecular Carbon Dioxide with Near-unity Faradaic Efficiency. *Angew Chem Int Edit* 2023, 62, e202213711.

Electronic Supplementary Material

High-temperature shock-induced transformation of bulk copper into single-atom catalyst

Renjie Fang[1,§], Ji Yang[1,§], Wei-Shen Song[1], Na Yang[2], Jie Ding[3], Jian-Feng Li[1] ✉, and Feng Ru Fan[1] ✉

[1] *State Key Laboratory of Physical Chemistry of Solid Surfaces, College of Chemistry and Chemical Engineering, Innovation Laboratory for Sciences and Technologies of Energy Materials of Fujian Province (IKKEM), Xiamen University, Xiamen 361005, China*

[2] *School of Materials and Energy, University of Electronic Science and Technology of China, Chengdu 611731, China*

[3] *Faculty of Chemistry and Food Chemistry & Center for Advancing Electronics Dresden (CFAED), Dresden University of Technology, Dresden 01062, Germany*

[§] *Renjie Fang and Ji Yang contributed equally to this work.*

Supporting information to https://doi.org/10.26599/NR.2025.94907300

Address correspondence to Jian-Feng Li, Li@xmu.edu.cn; Feng Ru Fan, frfan@xmu.edu.cn

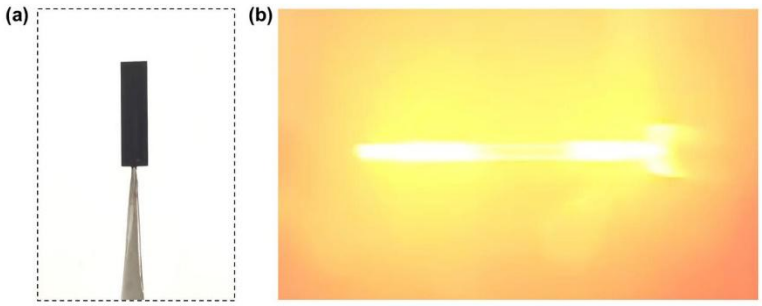

Figure S1. Images of Cu foil coated with N-C on both facet before (a) and (b) during pulse Joule heating.

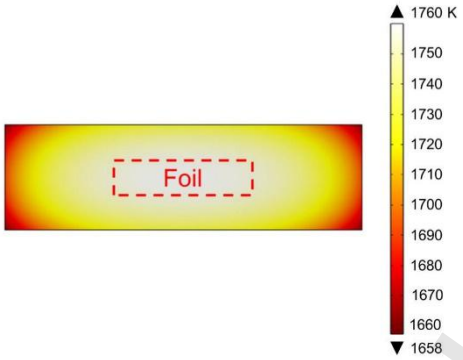

Figure S2. Planar temperature distribution during Cu-N-C-HTS synthesis using COMSOL Multi-Physics simulations. The central area of the carbon cloth in contact with the Cu foil (20×5 mm) demonstrates a uniform temperature distribution, with a maximum temperature variation of about 5 K.

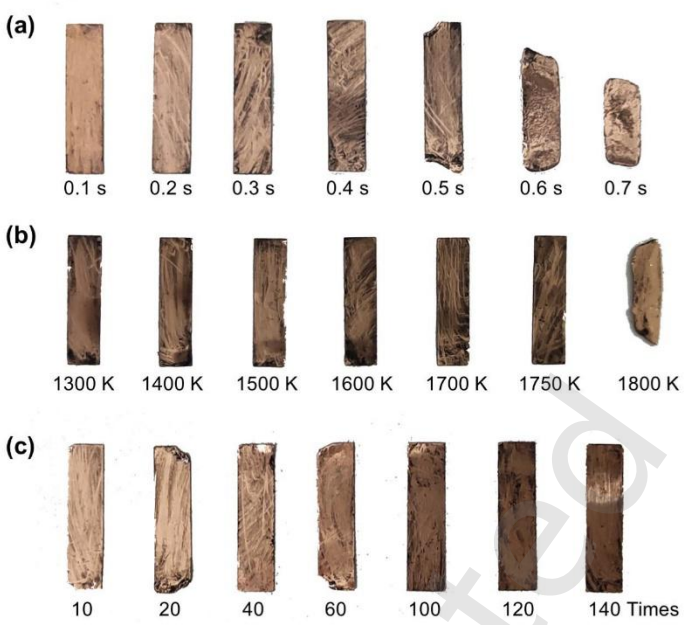

Figure S3. Images of Cu foils subjected to various conditions using a DC power source to manipulate pulse duration (a), times (b) and temperature (c) for controlled Cu loading in Cu-N-C-HTS.

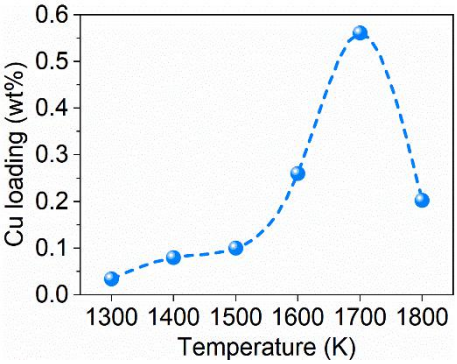

Figure S4. Heating temperature-dependent Cu mass weight profiles.

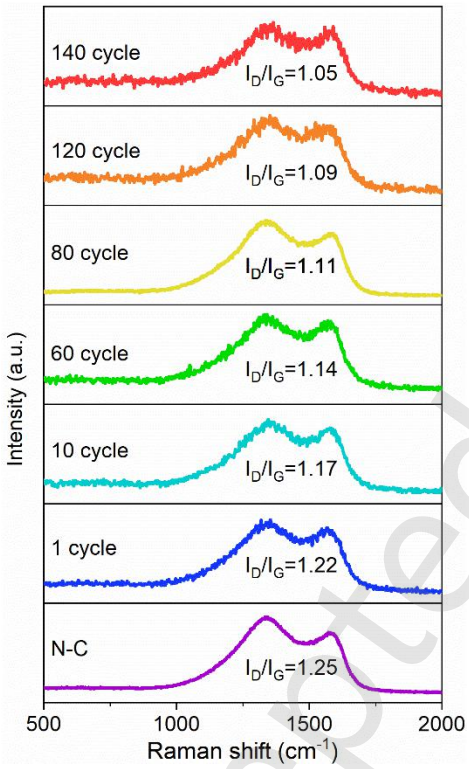

Figure S5. The Raman spectra of products obtained from different HTS cycles.

Raman spectroscopy was employed to analyze the defect levels of products derived from different HTS cycles by examining the intensity ratio of the D-band at 1350 cm^{-1} to the G-band at 1580 cm^{-1} (denoted as I_D/I_G), as shown in **Figure S5**. For the N-C support, an I_D/I_G value of 1.25 indicates a high density of nitrogen defects capable of anchoring excited copper atoms. Copper loading increased rapidly during 1 – 10 HTS cycles. However, as HTS cycles increased further, the I_D/I_G ratio progressively decreased, suggesting a reduction in nitrogen defect density in the support. Consequently, the number of captured copper atoms decreased, leading to a slower increase in copper loading between 10 and 80 HTS cycles. Beyond 80 cycles, the I_D/I_G values dropped to 1.11, 1.09, and 1.05 for 80, 120, and 140 HTS cycles, respectively, indicating a near-depletion of nitrogen defects, which hindered further significant increases in copper loading.

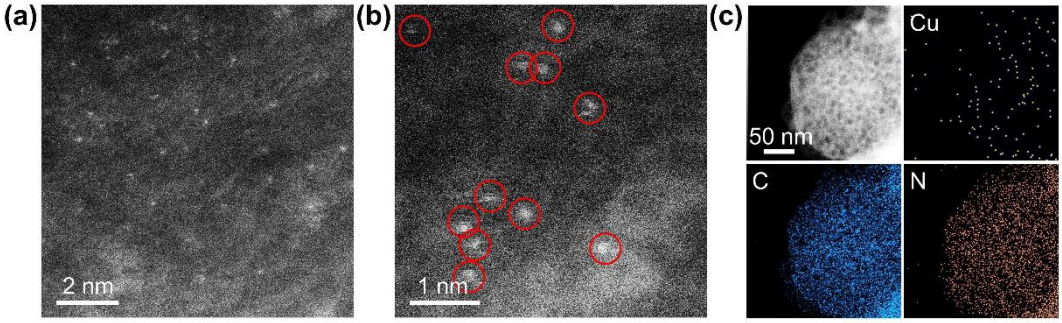

Figure S6. (a-b) HAADF-STEM images of Cu-N-C-HTS-140cycle, and **(c)** corresponding elemental mapping including Cu/C/N.

HAADF-STEM images of the product after 140 extreme HTS cycles confirmed that copper species could only be anchored by nitrogen defects, further substantiating the critical role of nitrogen defect density in determining copper loading.

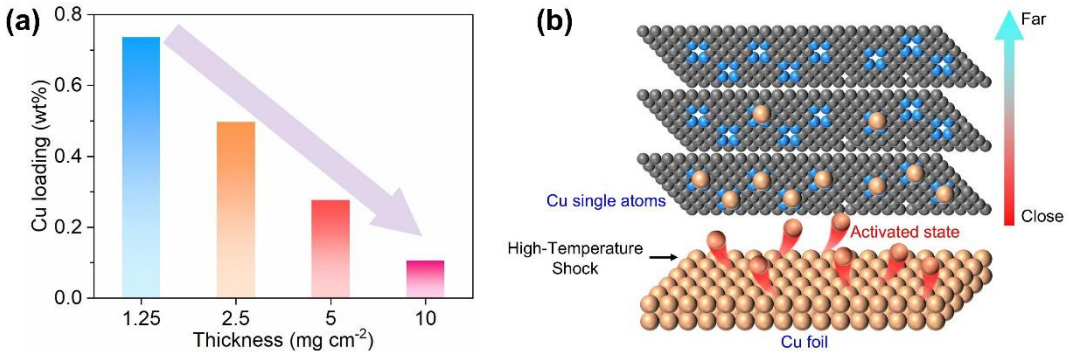

Figure S7. **(a)** Copper loading of HTS products prepared with different support deposition thicknesses on the copper foil surface. **(b)** Schematic illustration of the mechanism for capturing excited copper atoms at the solid-solid interface by the support.

As shown in **Figure S7A**, the copper loading in the support decreases significantly from 0.74 wt% to 0.10 wt% as the deposition thickness increases from 1.25 mg/cm^2 to 10 mg/cm^2. This indicates that thicker support deposition reduces the copper loading. Furthermore, this trend also highlights the non-uniform distribution of copper single atoms along the thickness direction of the support. This phenomenon aligns with AIMD simulation results, which reveal that the copper atom migration induced by pulsed high-temperature excitation occurs primarily at the solid-solid interface between the copper foil and the support. At this interface, copper atoms migrate to the support surface and are captured by nitrogen defects to form Cu-N-C-HTS. This mechanism suggests that the probability of capturing excited copper atoms is higher near the interface, resulting in higher copper loading in this region. Conversely, regions farther from the interface capture fewer copper atoms, leading to lower loading. This uneven distribution of copper single atoms along the thickness direction of the support is illustrated in **Figure S7B**.

Notably, thinner support deposition requires lower concentrations of the support-ethanol dispersion, which facilitates uniform spreading on the copper foil surface. This not only produces high-loading products but also benefits practical production processes.

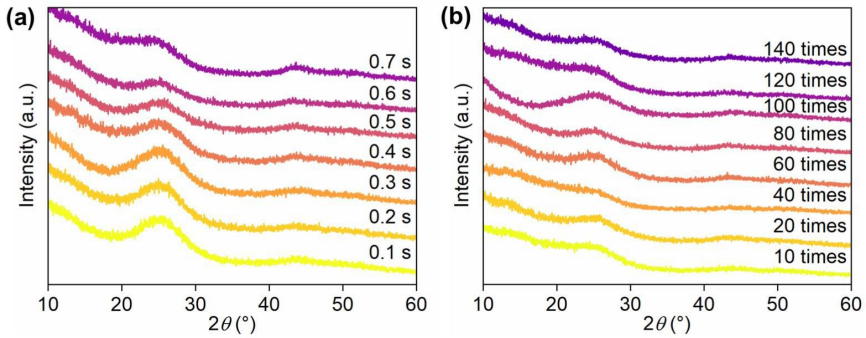

Figure S8. XRD patterns of Cu-N-C-HTS synthesized by HTS with **(a)** different pulse duration and **(b)** times.

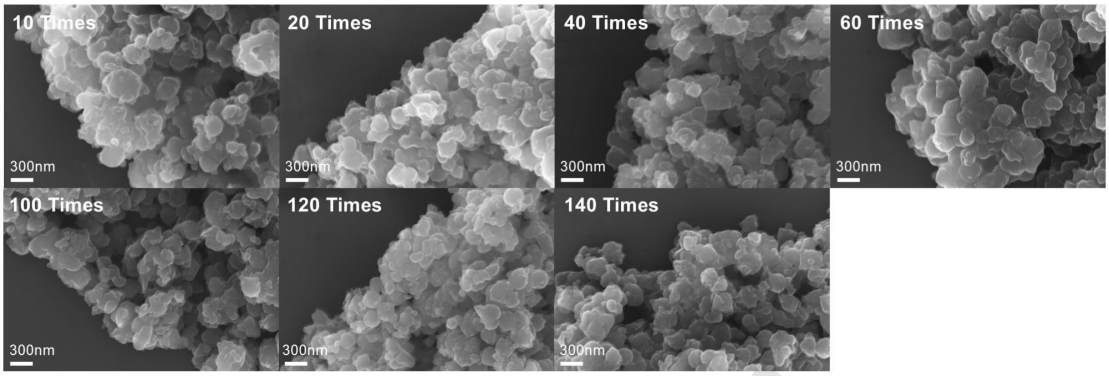

Figure S9. Scanning electron microscopy (SEM) images of Cu-N-C-HTS synthesized by HTS with different pulse duration.

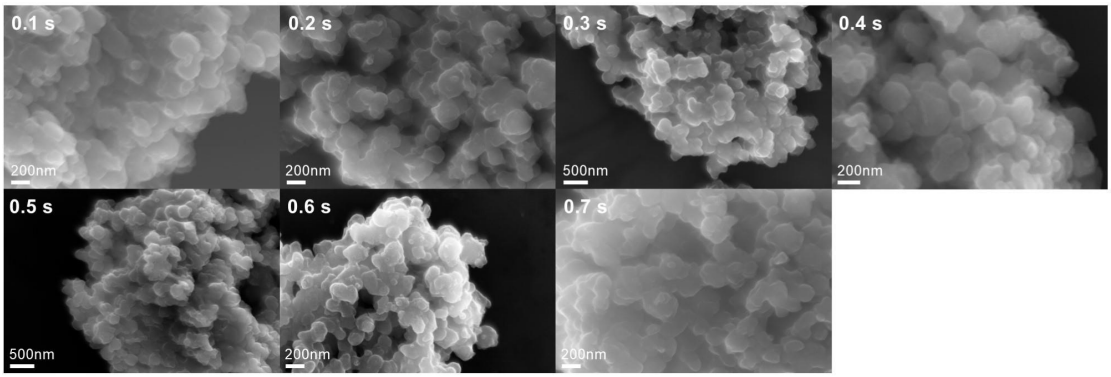

Figure S10. Scanning electron microscopy (SEM) images of Cu-N-C-HTS synthesized by HTS with different pulse times.

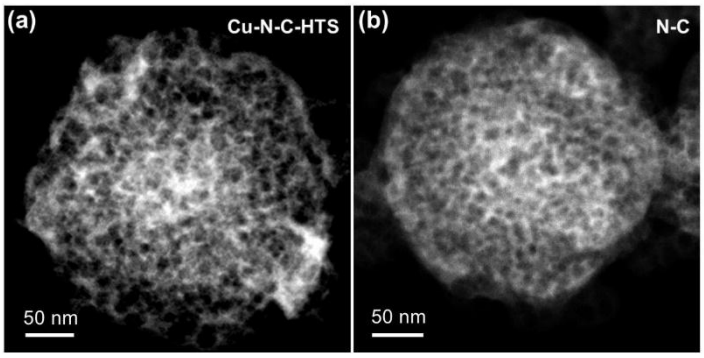

Figure S11. STEM images of **(a)** Cu-N-C-HTS and **(b)** N-C.

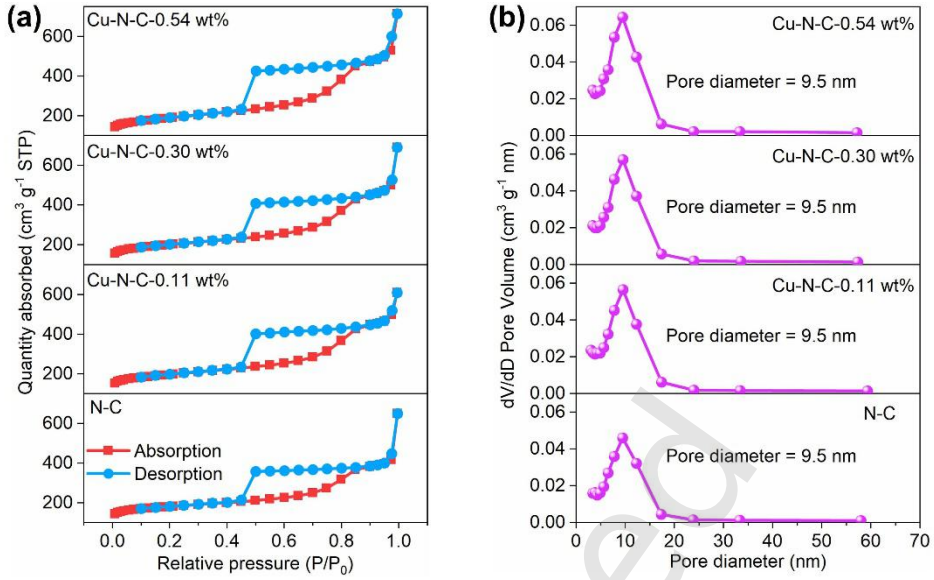

Figure S12. (a) N_2 adsorption-desorption isotherms of N-C and Cu-N-C-HTS catalysts with different copper loadings. **(b)** Pore diameter distribution of N-C and Cu-N-C-HTS catalysts with different copper loadings, determined using the Barrett-Joyner-Halenda (BJH) model.

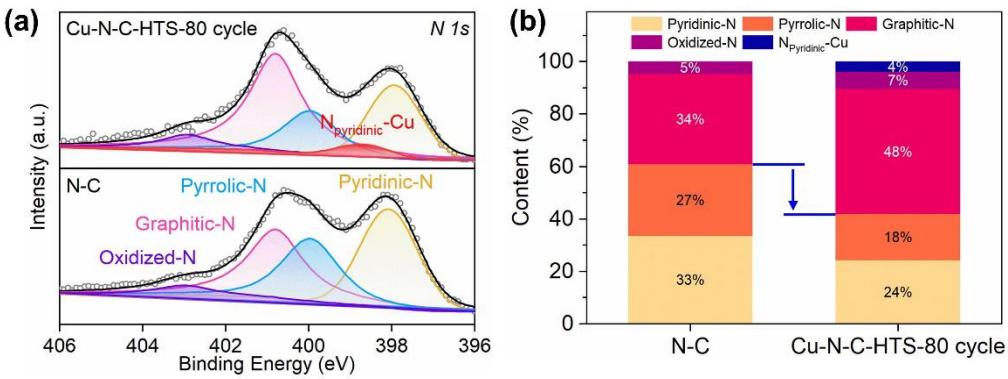

Figure S13. (a) N 1*s* X-ray photoelectron spectroscopy (XPS) spectra of Cu-N-C-HTS (top) and N-C (bottom). **(b)** The semi-quantitative analysis of nitrogen content.

Semi-quantitative analysis of the N 1s XPS deconvolution data showed that the proportion of Pyridinic N and Pyrrolic N, which are capable of forming coordination bonds with single copper atoms, decreased from 60% in the N-C support to 42% in the product after 80 HTS cycles. This also confirmed the declining number of nitrogen defects with increasing HTS cycles.

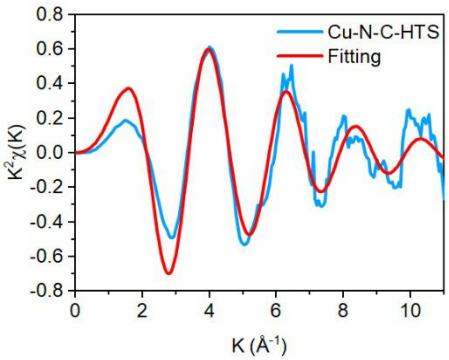

Figure S14. The corresponding FT-EXAFS fitting curve of Cu-N-C-HTS catalyst in the k space.

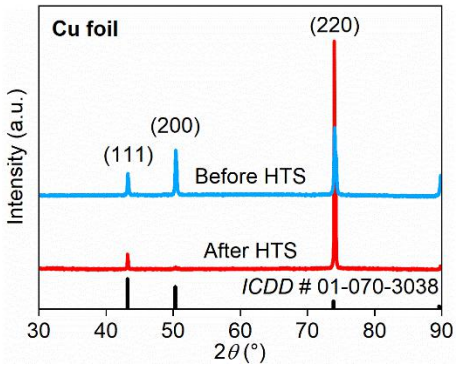

Figure S15. The comparison of XRD patterns between Cu foils before and after HTS synthesis.

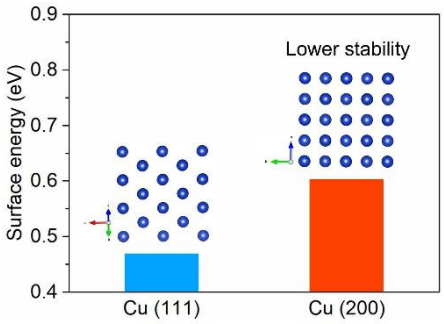

Figure S16. Comparison of surface energies between Cu (220) and Cu (111).

It is important to note that the disappearance of the Cu (200) peak in the XRD patterns is due to its lower structural stability compared to the Cu (111) plane. As shown in **Figure S16**, the surface energy of Cu (200) is approximately 0.603 eV, which is higher than that of Cu (111) at 0.469 eV. [1] Atoms on crystal planes with higher surface energy are more loosely packed, have weaker interactions, and exhibit lower thermodynamic stability. These planes are more prone to reconstruction, dissociation, or chemical reaction-induced destruction at high temperatures. Therefore, after HTS processing, the Cu (200) peak nearly disappears, reflecting its lower stability compared to the weakening intensity of the Cu (111) peak.

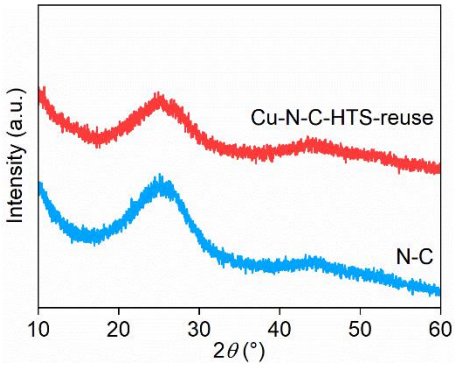

Figure S17. XRD patterns of Cu-N-C-HTS-reuse-20-times

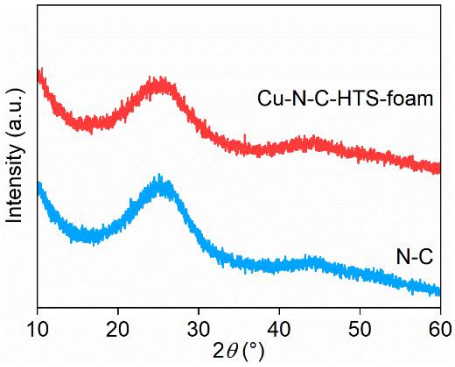

Figure S18. XRD patterns of Cu-N-C-HTS-foam.

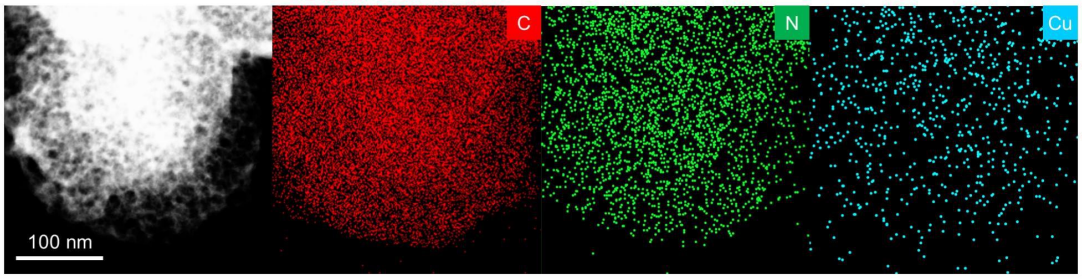

Figure S19. Energy dispersive spectroscopy (EDS) mapping of Cu-N-C-HTS (Cu foam).

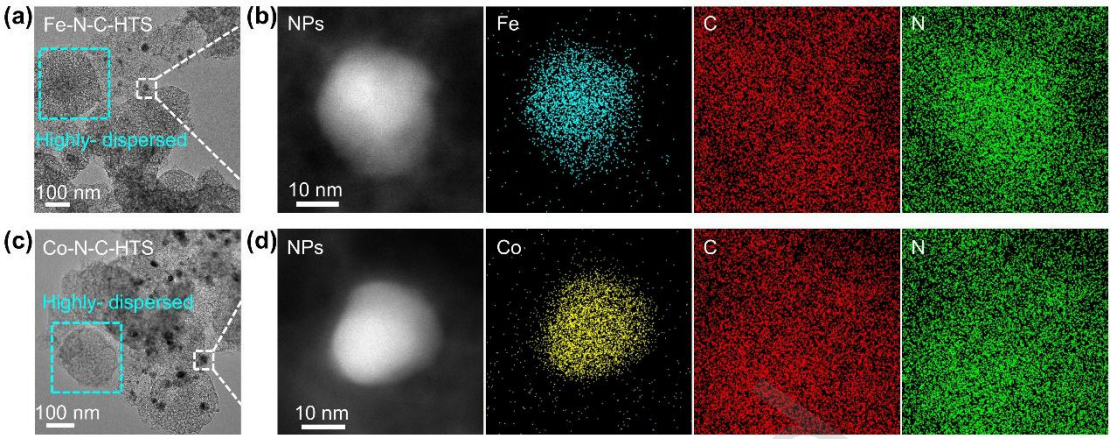

Figure S20. (a) TEM image of Co-N-C-HTS. **(b)** STEM image and corresponding EDS mapping of a metal particle region in Co-N-C-HTS. **(c)** TEM image of Fe-N-C-HTS. **(d)** STEM image and corresponding EDS mapping of a metal particle region in Fe-N-C-HTS.

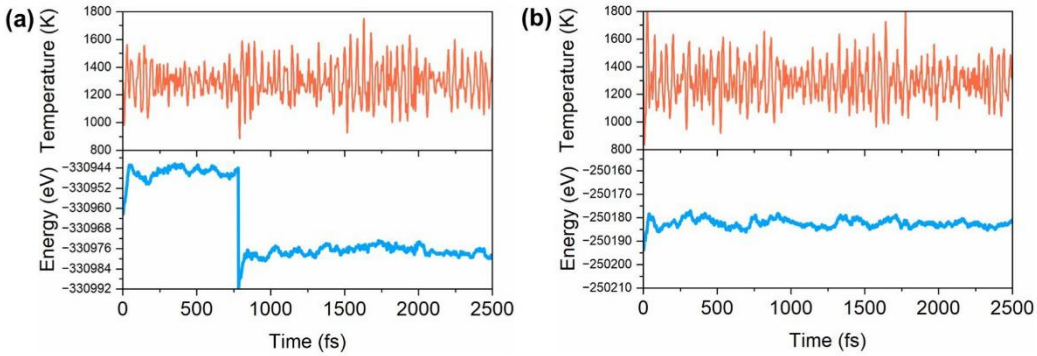

Figure S21. Variation of set temperature (up) and potential energy (bottom) of **(a)** Cu (111) and **(b)** Cu (220) with respect to the AIMD simulation time.

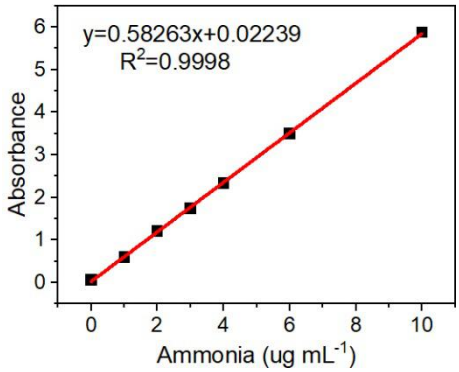

Figure S22. The concentration-absorbance calibration curves of ammonia.

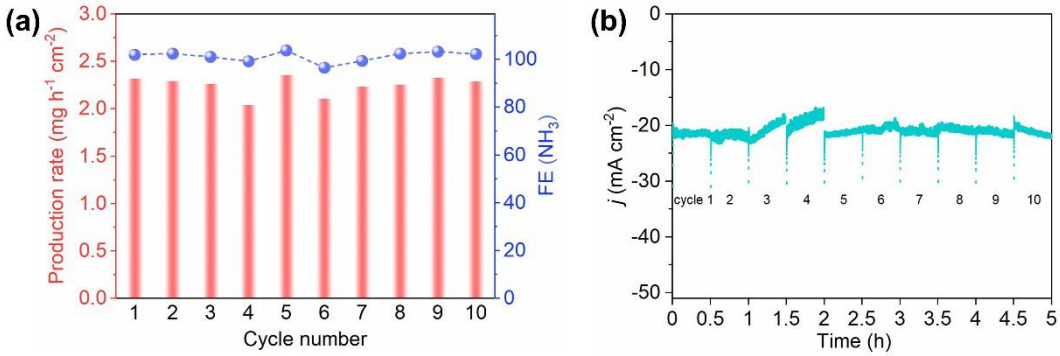

Figure S23. (a) Stability test showing the NH_3 yield and FE_{NH3} during continuous nitrite reduction at -0.6 V vs. RHE. **(b)** Current density profile during continuous nitrite reduction at -0.6 V vs. RHE, illustrating the durability of Cu-N-C-HTS over time.

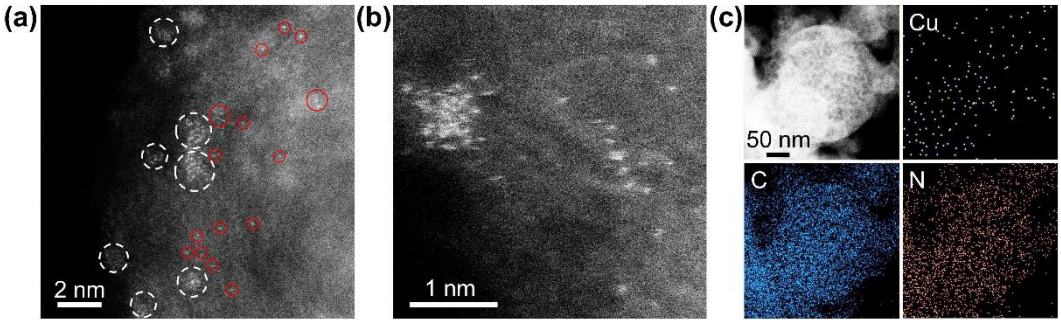

Figure S24. (a-b) HAADF-STEM images of Cu-N-C-HTS after the stability test for continuous nitrite reduction at -0.6 V vs. RHE. **(c)** Corresponding elemental mapping showing the distribution of Cu, C, and N.

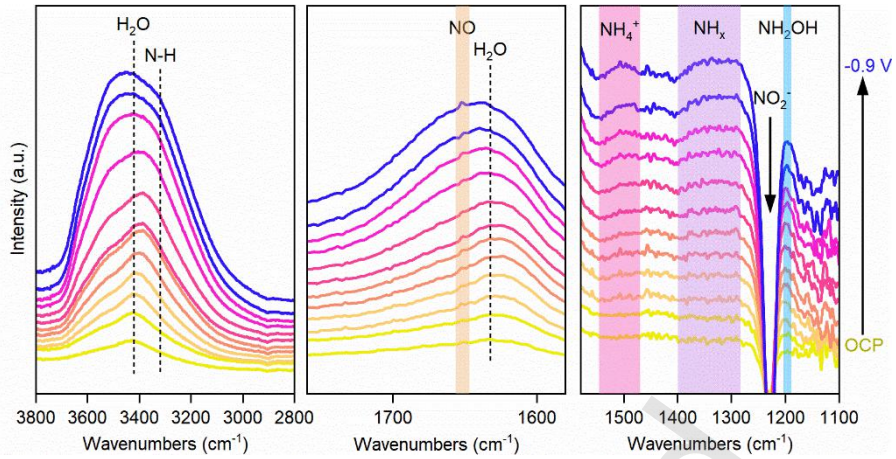

Figure S25. Potential-dependent in-situ FTIR spectra of Cu-N-C-HTS during the potential sweep from OCP to -0.9 V, with spectra collected at 0.1 V intervals.

As shown in **Figure S25**, during the negative scan from OCP to -0.9 V, the vibrational band associated with NO_2^- (approximately 1228 cm^{-1}) gradually intensifies with the increasing potential, indicating the continuous consumption of NO_2^- during the reaction.Additionally, as the potential increases, various hydrogenation intermediates emerge, including NO (≈1652 cm^{-1}), NH_x (≈1334 cm^{-1}), and NH_2OH (≈1196 cm^{-1}). Furthermore, NH_3-related peaks, including NH_4^+ (≈1500 cm^{-1}) and υ(N-H) (≈3318 cm^{-1}), appear, and their intensities progressively increase. These observations demonstrate that the NO_2RR process on Cu-N-C-HTS effectively generates a variety of hydrogenation intermediates, ultimately leading to the production of NH_3.

Table S1. The metal loading of Cu-N-C-HTS.

Shocking time (s)	0.1	0.3	0.4	0.5	0.6	0.7	
Cu loading (wt%)	0.179	0.231	0.297	0.581	0.486	0.453	
Temperature (K)	1300	1400	1500	1600	1700	1800	
Cu loading (wt%)	0.034	0.0792	0.1	0.26	0.561	0.202	
Shocking numbers	1	10	20	60	80	120	140
Cu loading (wt%)	0.11	0.395	0.45	0.507	0.581	0.6	0.55

Table S2. The surface analysis of N-C and Cu-N-C-HTS by XPS.

Catalysts	N-C	Cu-N-C-HTS
C (at%)	81.41	89.72
N (at%)	13.37	6.04
O (at%)	5.22	4.13
Cu (at%)	/	0.11
Pyridinic N (%)	33.32	24.09
$N_{Pyridinic}$-Cu (%)	/	4.00
Pyrrolic N (%)	27.37	17.73
Graphitic N (%)	34.48	47.61
Oxidized N (%)	4.84	6.58

TableS3. The best-fitted EXAFS results of Cu-N-C-HTS catalyst.

Sample	Shell	CN	R(Å)	σ^2 (10^{-2} Å^2)	ΔE_0 (eV)	r-factor (%)
Cu foil	Cu-Cu	12*	2.54	-	-	-
Cu-N-C-HTS	Cu-N	3.5	1.95	0.7	-10.1	0.2

CN is the coordination number for the absorber-backscatterer pair, R is the average absorber-backscatterer distance, σ^2 is the Debye-Waller factor, and ΔE_0 is the inner potential correction. * S_0^2 was fixed to 0.86 as determined from Cu foil fitting. The accuracies of the above parameters are estimated as CN, ±20%; R, ±1%; σ^2, ± 20%; ΔE_0 , ±20%. The data range used for data fitting in k-space (Δk) and R-space (ΔR) are 3.0-9.7 Å^{-1} and 1.0-1.8 Å, respectively.

Table S4. Metal loading of Cu-N-C-HTS (Cu foam), Fe-N-C-HTS and Co-N-C-HTS.

Cu foam	Shocking time (s)	0.1	0.2	0.3	
	Loading (wt%)	0.34	0.65	1.61	
Fe foil	Shocking time (s)	0.7	0.8	0.9	1.0
	Loading (wt%)	0.39	1.14	0.99	0.64
Co foil	Shocking time (s)	0.5	0.7	0.8	
	Loading (wt%)	0.82	1.29	3.5	

Table S5. Comparison of the optimum NH_3 yield rate and NH_3-Faradic efficiency (FE_{NH3}) for the recently reported NO_2RR electrocatalysts at ambient conditions.

Catalyst	Electrolyte	NH_3 yield rate ($\mu mol\ h^{-1}\ cm^{-2}$)	FE_{NH3} (%)	Potential (V vs RHE)	Ref.
Cu_3P NA/CF	0.1 M PBS (0.1 M $NaNO_2$)	95.7	91.2	-0.5	[2]
Cu/JDC/CP	0.1 M NaOH (0.1 M NO_2^-)	523.5	93.2	-0.6	[3]
Cu NW	0.1 M NaOH (0.1 M NO_2^-)	35.3	96.3	-0.7	[4]
CF@Cu_2O	0.1 M PBS (0.1 M $NaNO_2$)	441.8	94.2	-0.6	[5]
u-Cu	0.5 M Na_2SO_4 (0.1 M NO_2^-)	494.5	94.7	-0.7	[6]
Cu_1/Mo_2C	0.5 M NaOH (0.1 M NO_2^-)	472.9	91.5	-0.6	[7]
Cu_1/MnO_2	0.5 M Na_2SO_4 (0.1 M NO_2^-)	439.8	93.3	-0.7	[8]
Cu-N-C-HTS	**0.1 M KOH (0.1 M $NaNO_2^-$)**	**653.8**	**93.9**	**-1.2**	**This work**

References

[1] Da Silva, J. L. F.; Barreteau, C.; Schroeder, K.; Blügel, S., All-electron first-principles investigations of the energetics of vicinal Cu surfaces. *Phys Rev B* **2006**, 73 (12).

[2] Liang, J.; Deng, B.; Liu, Q.; Wen, G. L.; Liu, Q.; Li, T. S.; Luo, Y. L.; Alshehri, A. A.; Alzahrani, K. A.; Ma, D. W.; et al. High-efficiency electrochemical nitrite reduction to ammonium using a Cu3P nanowire array under ambient conditions. *Green Chem* **2021**, 23, 5487.

[3] Ouyang, L.; Yue, L. C.; Liu, Q.; Liu, Q.; Li, Z. R.; Sun, S. J.; Luo, Y. S.; Alshehri, A. A.; Hamdy, M. S.; Kong, Q. Q.; et al. Cu nanoparticles decorated juncus-derived carbon for efficient electrocatalytic nitrite-to-ammonia conversion. *J Colloid Interf Sci* **2022**, 624, 394.

[4] Zhang, Y. Y.; Wang, Y.; Han, L.; Wang, S. N.; Cui, T. D.; Yan, Y. F.; Xu, M.; Duan, H. H.; Kuang, Y.; Sun, X. M. Nitrite Electroreduction to Ammonia Promoted by Molecular Carbon Dioxide with Near-unity Faradaic Efficiency. *Angew Chem Int Edit* **2023**, 62, e202213711.

[5] Chen, Q. Y.; An, X. G.; Liu, Q.; Wu, X. Q.; Xie, L. S.; Zhang, J.; Yao, W. T.; Hamdy, M. S.; Kong, Q. Q.; Sun, X. P. Boosting electrochemical nitrite–ammonia conversion properties by a Cu foam@Cu2O catalyst. *Chem Commun* **2022**, 58, 517.

[6] Zhang, R. C.; Shang, S. Y.; Wang, F. Z.; Chu, K. Electrocatalytic reduction of nitrite to ammonia on undercoordinated Cu. *Dalton T* **2024**, 53, 3470.

[7] Wang, G. H.; Ma, R. Y.; Zhang, N. A.; Guo, Y. L.; Chu, K. Single-atom Cu anchored on Mo2C boosts nitrite electroreduction to ammonia. *Chem Commun* **2023**, 59, 13887.

[8] Wan, Y. Y.; Du, W. Y.; Chen, K.; Zhang, N. A.; Chu, K. Electrocatalytic nitrite-to-ammonia reduction on isolated Cu sites. *J Colloid Interf Sci* **2023**, 652, 2180.

Videos

Video S1. AIMD simulations reveal the structural evolution from copper foil to the single-atom in the N-C/Cu (111) structure during HTS.

Video S2. AIMD simulations reveal the structural evolution from copper foil to the single-atom in the N-C/Cu (220) structure during HTS.